

# The Open DAC 2023 Dataset and Challenges for Sorbent Discovery in Direct Air Capture

Anuroop Sriram,<sup>\*,†</sup> Sihoon Choi,<sup>†,‡</sup> Xiaohan Yu,<sup>‡</sup> Logan M. Brabson,<sup>‡</sup> Abhishek Das,<sup>†</sup> Zachary Ulissi,<sup>†</sup> Matt Uyttendaele,<sup>†</sup> Andrew J. Medford,<sup>\*,‡</sup> and David S. Sholl<sup>\*,‡,¶</sup>

<sup>†</sup>*Fundamental AI Research, Meta AI, Meta, Menlo Park, CA, USA*

<sup>‡</sup>*School of Chemical and Biomolecular Engineering, Georgia Institute of Technology, Atlanta, GA, USA*

<sup>¶</sup>*Oak Ridge National Laboratory, Oak Ridge, TN, USA*

E-mail: anuroops@meta.com; ajm@gatech.edu; shollds@ornl.gov

## Abstract

New methods for carbon dioxide removal are urgently needed to combat global climate change. Direct air capture (DAC) is an emerging technology to capture carbon dioxide directly from ambient air. Metal-organic frameworks (MOFs) have been widely studied as potentially customizable adsorbents for DAC. However, discovering promising MOF sorbents for DAC is challenging because of the vast chemical space to explore and the need to understand materials as functions of humidity and temperature. We explore a computational approach benefiting from recent innovations in machine learning (ML) and present a dataset named Open DAC 2023 (ODAC23) consisting of more than 38M density functional theory (DFT) calculations on more than 8,400 MOF materials containing adsorbed CO<sub>2</sub> and/or H<sub>2</sub>O. ODAC23 is by far the largest dataset of MOF adsorption calculations at the DFT level of accuracy currently available. In addition to probing properties of adsorbed molecules, the dataset is a rich source of information on structural relaxation of MOFs, which will be useful in many contexts beyond specific applications for DAC. A large number of MOFs with promising properties for DAC are identified directly in ODAC23. We also trained state-of-the-art ML models on this dataset to approximate calculations at the DFT level. This open-source dataset and our initial ML models will provide an important baseline for future efforts to identify MOFs for a wide range of applications, including DAC.

## Keywords

Direct air capture, metal organic frameworks, carbon capture, density functional theory, datasets, machine learning, graph convolutions, force field

# Introduction

Annual anthropogenic carbon emissions reached nearly 36 billion tonnes in 2020, and the atmospheric carbon dioxide concentration has increased  $\sim 50\%$  since preindustrial times to approximately 420 ppm.<sup>1</sup> Rising CO<sub>2</sub> levels have motivated the development of carbon capture and sequestration (CCS) technologies to combat the effects of emissions on global climate change.<sup>2</sup> Direct air capture (DAC) is an emerging technology with the potential for distributed capture and negative emissions.<sup>3</sup> DAC operates at ambient conditions and avoids impurities that are common for point source capture of CO<sub>2</sub>, but the low concentration of CO<sub>2</sub> requires the movement of large volumes of air and strong adsorption of CO<sub>2</sub>.<sup>4</sup> Many current DAC absorbents, such as liquid amines and solid alkali hydroxides, strongly bind CO<sub>2</sub> through chemisorption, requiring energy-intensive regeneration of the sorbent.<sup>5,6</sup> Metal-organic frameworks (MOFs) are a promising class of alternative sorbent materials for DAC allowing regeneration at relatively low temperatures. In contrast to sorbents such as alkali hydroxides, MOFs are modular, flexible, and highly tunable, and they possess remarkably high porosities, low densities, and long-range order.<sup>7</sup> The chemical tunability and long-range order make MOFs worthy of high-throughput computational screening studies.

Computational materials design is a promising strategy for DAC sorbents.<sup>8</sup> Design of efficient DAC processes may require tailoring of materials to the specifics of the air temperature and humidity conditions in a given environment or the temperature/pressure swings that are required to keep energy consumption low.<sup>9</sup> This is particularly true of DAC processes that seek to leverage air movement and energy content of existing systems such as heating, ventilation, and air conditioning.<sup>10</sup> The consideration of humidity is particularly important, since dehumidifying air requires significant energy input, the presence of H<sub>2</sub>O can result in competitive adsorption even at low relative humidities, and humidity can in some cases cause adsorbent degradation over time.<sup>11-14</sup> The availabil-

ity of large datasets of MOFs and other solid sorbent materials can facilitate identification of specific materials or chemical moieties that are well suited for the specific conditions of a given DAC process.<sup>15,16</sup>

High-throughput computational studies and machine learning (ML) techniques are already a common practice in the screening and discovery of MOFs and other reticular materials.<sup>12,17-25</sup> There are several large databases of MOF<sup>26-31</sup> and zeolite structures<sup>32</sup> and multiple computational toolkits<sup>33-37</sup> and ML models<sup>23,38-43</sup> to analyze and predict the adsorption properties of these materials. However, there are several key limitations to the existing body of work. First, because of the computational costs involved, many studies rely on empirical force field (FF) models for predicting adsorption properties. Inaccuracies associated with FFs can lead to both qualitative and quantitative inconsistencies in the prediction of material performance, particularly in the case of open-metal sites (OMS) or defects where covalent bonding or complexation occurs.<sup>17,44-49</sup> There are several large databases of density functional theory (DFT) calculations for MOF materials,<sup>27,31</sup> but to date these are focused only on the MOF structure and do not include adsorption data. Second, many existing databases and studies of CO<sub>2</sub> adsorption focus only on adsorption of CO<sub>2</sub>, neglecting the possibility of competition with H<sub>2</sub>O.<sup>11,50-53</sup> Failure to consider competitive adsorption will strongly limit the ability to predict materials for practical DAC processes, where bicomponent CO<sub>2</sub>/H<sub>2</sub>O isotherms are required. Accurately modeling H<sub>2</sub>O adsorption with classical FFs is challenging due to the complex physical properties of water.<sup>54-57</sup> Third, many computational databases and studies focus on hypothetical materials,<sup>28,30,58,59</sup> which leads to practical challenges in the synthesis and experimental testing of new predicted materials. Finally, most datasets are restricted to pristine materials. In reality, MOFs will contain a wide range of defects that may govern their adsorption properties under practical conditions.<sup>60,61</sup> New materials can also be created by inserting defects in MOFs via so-called defect-engineering.<sup>62</sup> Large datasets of high-quality DFT simulations of

mixed CO<sub>2</sub> and H<sub>2</sub>O adsorption on realistic pristine and defective MOFs are needed to address these limitations.

ML is also a well-established approach in the discovery of MOFs and other nanoporous materials. ML models have been applied to directly predict adsorption properties and isotherms of MOFs based on their physical and chemical structure.<sup>23,41–43,63–65</sup> Descriptors based on the porosity, chemical constituents, and energy landscape of probe adsorbates in MOFs have been combined with a range of regression and classification models to provide predictions of gas loadings,<sup>23,42,66,67</sup> Henry’s constants,<sup>40,68</sup> and temperature-dependent isotherms.<sup>63,64</sup> Neural networks have been used to predict MOF properties and perform inverse design tasks to identify MOF materials with high thermal stability<sup>58,69</sup> and strong or selective CO<sub>2</sub> adsorption.<sup>43,59,65</sup> ML models have also been trained to provide insight into synthesizability and stability of MOFs and zeolites.<sup>70–74</sup> However, the training data required for many of these properties, such as adsorption isotherms, are generated using classical FFs, which have been shown to exhibit systematic errors.<sup>45</sup> Efforts to train ML models that can directly emulate DFT data for MOFs are more limited.<sup>43</sup> The ability to use ML models to directly replace FFs in MOFs has the potential to enhance many of the prior efforts.

In this work, we introduce the Open DAC 2023 (ODAC23) dataset to address these challenges. The dataset consists of adsorption energies for CO<sub>2</sub>, H<sub>2</sub>O, and mixtures thereof on ~8K MOFs, amounting to a total of ~176K adsorption energies and ~38M single-point calculations (Fig. 1). All calculations were performed using DFT with the PBE+D3 exchange correlation functional, ensuring that covalent and electrostatic interactions are treated quantum mechanically and van der Waals interactions are included with well-established empirical accuracy. Approximately 76K adsorption energies involve MOFs that have missing linker defects, providing a route to predicting the role of defects. The dataset is used to train and evaluate state-of-the-art ML models for the prediction of adsorption energies and atomic forces

using approaches developed for the Open Catalyst Project.<sup>75</sup> In addition, we include several out-of-domain datasets taken from the extended CoRE MOF database<sup>58,76</sup> to evaluate the ability of the trained models to generalize to unseen topologies and linker chemistries. We expect that this dataset and the associated infrastructure will accelerate the development of MOF materials for DAC by providing a common dataset that far exceeds the size of any currently available dataset, establishing well-defined standards and benchmarks for development of new ML models, and providing accessible pre-trained ML models that enable routine prediction of mixed CO<sub>2</sub> and H<sub>2</sub>O adsorption on MOFs at an accuracy that approaches DFT.

The ODAC23 dataset is publicly available at the OpenDAC website<sup>i</sup>. All of our trained ML models and training code are available in the OCP repository<sup>ii</sup>.

## Scope and Structure of the ODAC23 Dataset

Enormous numbers of hypothetical MOF structures exist, as illustrated by the hypothetical MOF database (hMOF) of Wilmer *et al.*, which contains 138,000 structures.<sup>28</sup> Several other MOF databases have been developed, including the Topologically Based Crystal Constructor (ToBaCCo) database of 13,512 MOFs with 41 unique topologies developed by Colón *et al.*<sup>30</sup> Perhaps most importantly, Chung *et al.* developed the Computation-Ready, Experimental (CoRE) MOF database<sup>26</sup> and its 2019 expansion<sup>27</sup> from experimentally synthesized structures in the Cambridge Structural Database (CSD).<sup>77</sup> The CoRE MOF database has been the foundation of many studies and extensions, including assignment of DFT-derived point charges,<sup>78</sup> more thorough cleaning by removal of structures with misbonded or overlapping atoms,<sup>79</sup> and the QMOF database of DFT-derived properties of many CoRE MOF structures.<sup>31</sup>

<sup>i</sup><https://open-dac.github.io/>

<sup>ii</sup><https://github.com/Open-Catalyst-Project/ocp>

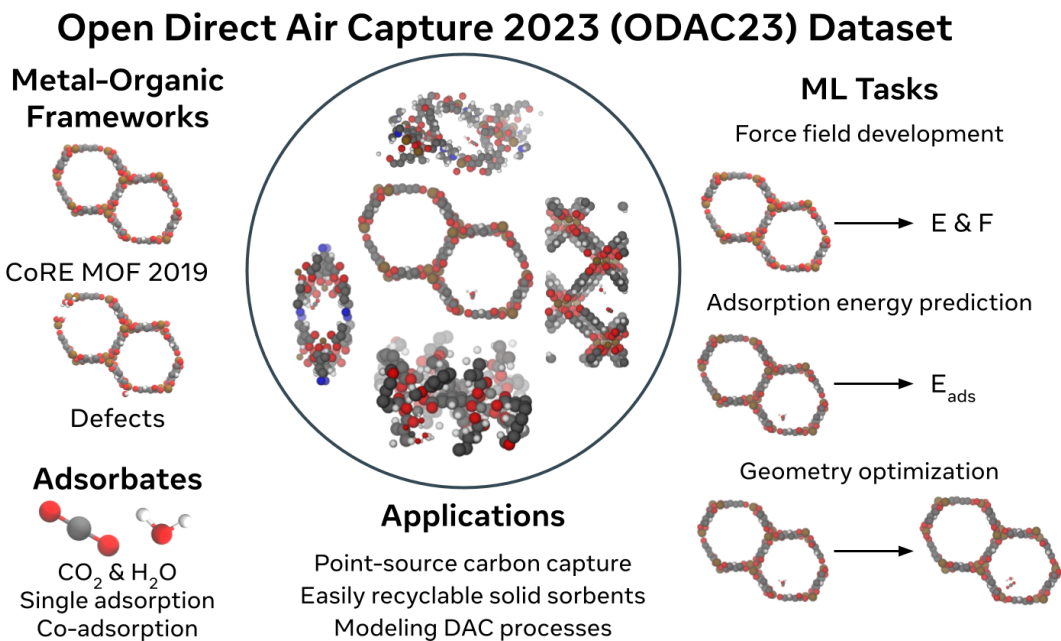


Figure 1: Materials, adsorbates, tasks, and potential applications of the ODAC23 dataset. Images are randomly sampled from the dataset.

The Open DAC dataset uses the CoRE MOF 2019 work as a starting point. This approach is beneficial because the data are readily available and the origin of each MOF in the database in an experimentally reported synthesis partially addresses concerns surrounding practicality when considering candidate MOFs for experimental testing. The CoRE MOF database has also been shown to be more chemically diverse than larger databases of hypothetical materials, which is beneficial for training transferable and generalizable ML models.<sup>80</sup> The CoRE MOF 2019-ASR database contains 12,020 unique structures with accessible data. We only consider MOFs that contain fewer than 1,000 atoms in the unit cell due to computational cost. MOFs with a pore limiting diameter (PLD) of less than 3.3 Å are excluded because a CO<sub>2</sub> molecule (kinetic diameter of 3.3 Å) may experience kinetic limitations in entering such small pores.<sup>27</sup> With these limitations, 8,803 MOFs serve as our starting point for DFT relaxation.

We used the Perdew-Burke-Ernzerhof functional<sup>81</sup> with a D3 dispersion correction<sup>82,83</sup> (PBE-D3) for all calculations. The generalized gradient approximation (GGA) approach was chosen over more accurate methods such as hy-

brid functionals or coupled cluster techniques because of the size and diversity of the dataset. Nazarian *et al.* showed that several different functionals and dispersion corrections perform similarly when making structural and partial charge predictions on a chemically diverse set of MOFs.<sup>78</sup> We did not include a Hubbard  $U$  correction. Without this correction, PBE systematically overpredicts binding energies on open-metal sites, but  $U$  values are empirical and are difficult to find for every metal type.<sup>84</sup> We ran calculations as spin polarized to capture spin effects associated with open metal sites. Our work ultimately seeks to push the baseline description of MOFs for DAC from classical FFs to the PBE-D3 level of theory, so we prioritized consistency across a very large number of calculations rather than absolute accuracy.

The ODAC23 dataset consists of complete relaxation trajectories of CO<sub>2</sub>, H<sub>2</sub>O, and mixtures of CO<sub>2</sub> and H<sub>2</sub>O on MOF structures derived from the CoRE MOF database. We include two classes of MOF frameworks: *pristine* frameworks and *defective* structures with missing linker defects systematically added.<sup>85</sup> Pristine MOF structures are obtained from the CoRE MOF database without further modification. Approximately 66% of the pristine MOFs

include frameworks with open metal sites. To test generalizability, we also included 114 “ultrastable” MOFs from Nandy *et al.* created by fragmenting and recombining linkers and nodes from the original CoRE MOF database.<sup>76</sup> The final dataset includes a total of 4,942 pristine MOFs and 3,470 defective MOFs with defect concentrations ranging from 1-16%. The MOFs contain a diverse set of 57 metals, with Zn, Cu, and Cd being the most common, and include a mix of monometallic (89%), bimetallic (10.7%), and trimetallic (< 1%) frameworks. The abundance of various metals is provided in Fig. S1, and the most common linkers are listed in Table S2. The adsorbates were initially placed using classical FFs and Monte Carlo sampling, with  $\sim$ 2-6 placements per framework. The selection of MOFs and adsorption configurations included in the final set are established by pragmatic constraints and practical considerations. In total, the dataset consists of over 170K converged adsorption energies and nearly 40M single point calculations, corresponding to over 400M core-hours of compute time. Details are provided in the Methods section.

The Open DAC 2023 (ODAC23) dataset has been designed to allow training of ML models to approximate DFT calculations, similar to previous work in heterogeneous catalysis (OC20 and OC22).<sup>75,86</sup> We use the same three task definitions used in the OC20 work. These tasks are briefly summarized below, and we refer the reader to the OC20 paper<sup>75</sup> for more detailed descriptions.

In each task, the input structure is a unit cell periodic in all directions containing a MOF with one or more adsorbates. The ground truth targets of forces, energies, and relaxed structures were all calculated using DFT. For energy targets, we used a non-relaxed adsorption energy:

$$\tilde{E}_{\text{ads}} = E_{\text{system}} - E_{\text{MOF}} - n_{\text{CO}_2} E_{\text{CO}_2} - n_{\text{H}_2\text{O}} E_{\text{H}_2\text{O}} \quad (1)$$

where  $E_{\text{system}}$  is the energy of the MOF and adsorbates,  $E_{\text{MOF}}$  is the energy of the relaxed MOF structure without an adsorbate,  $n_i$  is the number of adsorbate  $i$  and  $E_i$  is the energy of adsorbate  $i$  in the gas phase. The tilde on  $\tilde{E}_{\text{ads}}$

denotes that  $E_{\text{system}}$  is not necessarily a relaxed structure. In specific cases where  $E_{\text{system}}$  is relaxed, the tilde is dropped and the adsorption energy is denoted as  $E_{\text{ads}}$ . More details are provided in the Methods section.

The energies of these MOF+adsorbate structures were used to train models for three tasks:

1. **Structure to Total Energy and Forces (S2EF)** takes a structure as input and predicts  $\tilde{E}_{\text{ads}}$  of the system as well the force on each atom. This task is analogous to training a force field for all atoms in the system.
2. **Initial Structure to Relaxed Energy (IS2RE)** takes an initial guess structure as input and predicts  $E_{\text{ads}}$  of its relaxed structure. This task is analogous to predicting an adsorption energy from an initial structure.
3. **Initial Structure to Relaxed Structure (IS2RS)** takes an initial guess structure as input and predicts the relaxed position of each atom. This task is analogous to geometry optimization.

The S2EF task is the most general, and an S2EF model can be used to complete the IS2RS and IS2RE tasks. The dataset is organized by task and train/test splits. For each task, the data is split into a training set, testing set, and validation set. These in-domain (id) sets are randomly sampled from the full dataset derived from CoRE MOF, but are stratified by MOF framework to ensure that all defective structures are in the same set as the pristine structure from which they are generated. Four out-of-domain (ood) sets are included. The “big” ood set corresponds to MOFs from CoRE with over 500 atoms in their unit cell (testing the ability to generalize to larger structures). The “linker”, “topology” ood sets contain linkers and topologies not included in the training data, selected from MOFs in the ultrastable MOF dataset of Nandy *et al.*<sup>76</sup> The “linker and topology” ood set contains MOFs from the ultrastable MOF dataset that contain both unseen linkers and topologies. The number of

Table 1: Overview of ODAC23 dataset organised by dataset split, number of MOF frameworks, and number of DFT calculations.

Split	# Pristine MOFs	# Defective MOFs	# Total MOFs	# Total DFT Relaxations	# Total DFT Single Points
train	4,537	3,287	7,824	162,224	35,871,295
val	121	71	192	3,998	839,565
test-id	120	93	213	4,669	973,515
test-ood (big)	66	19	85	1,768	381,219
test-ood (linker)	28	0	28	1,182	287,125
test-ood (topology)	55	0	55	1,612	472,256
test-ood (linker & topology)	15	0	15	579	158,773
<b>Total</b>	<b>4,942</b>	<b>3,470</b>	<b>8,412</b>	<b>176,032</b>	<b>38,983,748</b>

MOF structures and DFT calculations in each set is provided in Table 1, and a more detailed breakdown based on adsorbate type is provided in S1. Fig. 2 illustrates this detailed distribution across adsorbate types split by task. Further details are described in the Methods section.

## Identification of Selective CO<sub>2</sub> Adsorption Sites

We used our DFT calculations to directly search for MOFs that are potentially interesting for DAC following the criteria suggested by Findley and Sholl<sup>12</sup> that the adsorption energy of CO<sub>2</sub> is  $< -0.5$  eV (with our sign convention, more negative binding energies correspond to more favorable binding) and that the adsorption energy of CO<sub>2</sub> needs to be more favorable than that for H<sub>2</sub>O. Materials not satisfying the first criterion are unlikely to bind sufficient quantities of CO<sub>2</sub> at the dilute concentrations relevant for DAC, and materials not satisfying the second criterion are likely to adsorb far more water from air than CO<sub>2</sub>. In the following analysis, we compared the lowest adsorption energy of all computed configurations for each MOF + adsorbate case. We neglected cases with  $|E_{\text{ads}}/(n_{\text{CO}_2} + n_{\text{H}_2\text{O}})| > 2$  eV because we suspect these cases are unphysical.

Fig. 3a and b compare the CO<sub>2</sub> and H<sub>2</sub>O adsorption energies in each pristine and defective MOF from our DFT calculations. As expected, most of the MOFs bind water more favorably than CO<sub>2</sub>. However, 135 of the 5,079 pristine MOFs bind CO<sub>2</sub> strongly and have higher affinity for CO<sub>2</sub> than for H<sub>2</sub>O. The top 10 pristine MOFs identified by our DFT calculations with

the highest values of  $|E_{\text{ads}}(\text{CO}_2) - E_{\text{ads}}(\text{H}_2\text{O})|$  are tabulated in Table S3.

Several screenings of the CoRE MOF database for CO<sub>2</sub> capture in the presence of water have been conducted previously.<sup>87,88</sup> Here, we compare our promising MOFs with two previous studies where the adsorption energies of CO<sub>2</sub> and H<sub>2</sub>O in CoRE MOFs are available. Findley and Sholl performed a similar screening of CoRE MOFs using FF methods, finding no cases that satisfied the criteria stated above.<sup>12</sup> The observation that our DFT calculations of analogous quantities identified many interesting materials suggests that the generic FFs used previously are insufficiently accurate. Kancharlapall and Snurr recently screened the CoRE MOF 2019 database with a combination of FF and DFT calculations, using somewhat different selection criteria.<sup>89</sup> Kancharlapall and Snurr also found that FF-based calculations failed to identify MOFs that satisfy our criteria. They further analyzed a subset of their most promising structures using DFT, with a slightly different workflow than we use for ODAC23. We find that 17 materials identified by Kancharlapall and Snurr also appear in the ODAC23 dataset, though we find that 7 of these materials bind H<sub>2</sub>O more strongly than CO<sub>2</sub> and the remaining 10 MOFs bind CO<sub>2</sub> weakly ( $E_{\text{ads}}(\text{CO}_2) \geq -0.5$  eV), indicating that they may not be promising for DAC.

In addition to considering the adsorption of single CO<sub>2</sub> and H<sub>2</sub>O molecules, we also used DFT to probe the co-adsorption of CO<sub>2</sub> and H<sub>2</sub>O in MOFs. With the resulting co-adsorption energies, we computed the adsorbate-adsorbate interaction energies associated with removing both molecules from the co-adsorbed state, denoted  $E_{\text{inter,mol}}^{\text{1st}}$ , for each

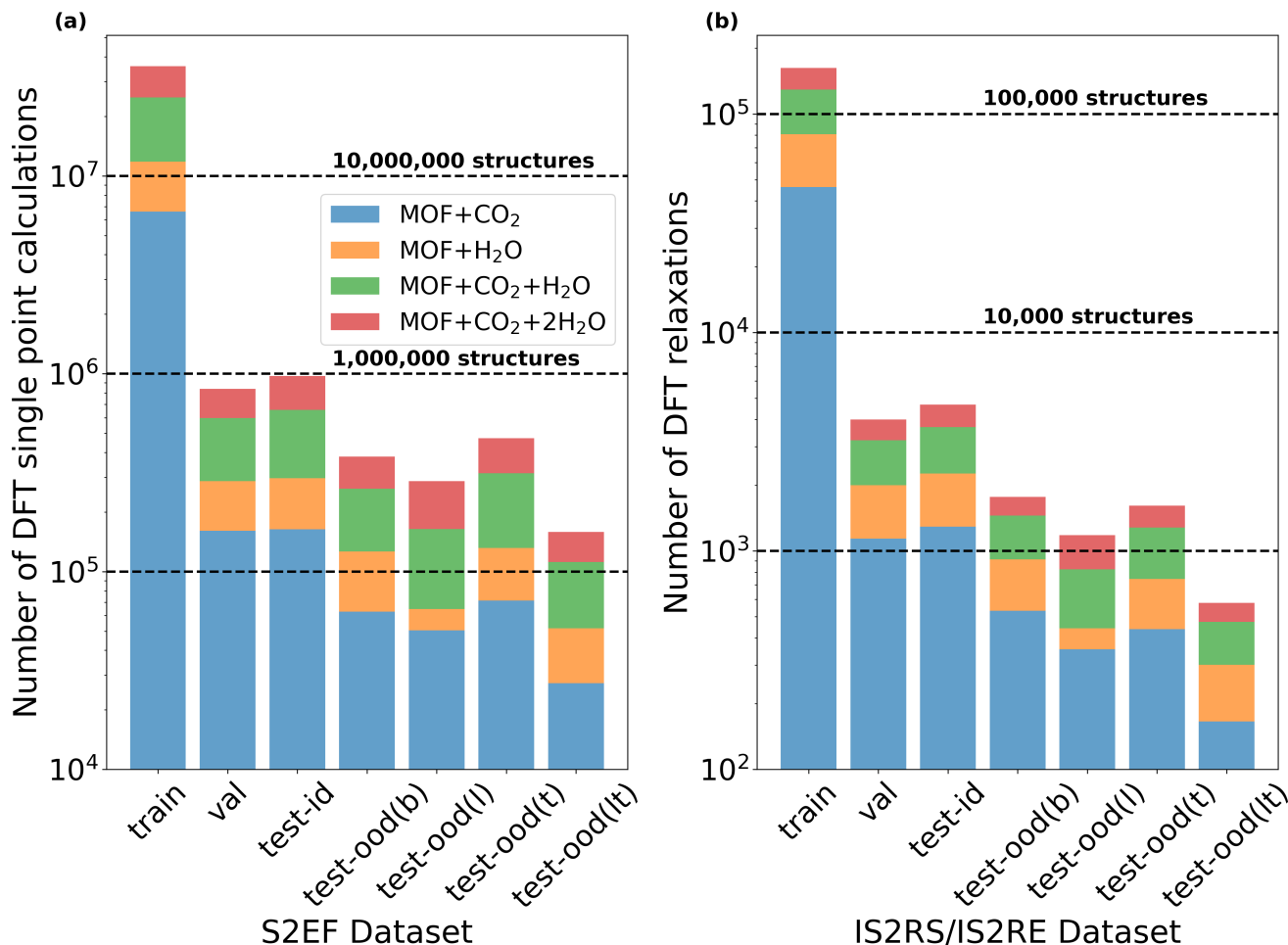


Figure 2: Distribution of the number of MOF+adsorbate DFT calculations for the (a) S2EF and (b) IS2RS/IS2RE tasks on a logarithmic scale. The horizontal lines emphasize the size of the dataset.

MOF using equation (6). For the 10 MOFs listed in Table S3 there are three distinct scenarios for this quantity. In a simple case like ZIDBEV,  $E_{\text{inter.mol}}^{\text{1st}} = 0$  eV is small relative to the single molecule adsorption energies, so co-adsorption can be approximated in a simple way as separate adsorption of the two molecules. For MOFs with negative adsorbate-adsorbate interaction energies like IMAGAG ( $E_{\text{inter.mol}}^{\text{1st}} = -0.64$  eV), co-adsorption of CO<sub>2</sub> and H<sub>2</sub>O is strongly favored relative to adsorption of the individual molecules. Positive adsorbate-adsorbate interaction values such as those seen for IPIDUH ( $E_{\text{inter.mol}}^{\text{1st}} = 1.04$  eV) and TUGTAR ( $E_{\text{inter.mol}}^{\text{1st}} = 0.51$  eV) indicate the co-adsorption is much less favorable than adsorption of isolated molecules. In some cases the first adsorbate-adsorbate interaction energies are strongly nonzero (e.g. KOQLUZ,

$E_{\text{inter.mol}}^{\text{1st}} = -2.31$  eV), suggesting that rearrangement of the MOF structure occurred in the co-adsorbed case that was not observed for the individual adsorbed molecules.

For the CO<sub>2</sub> + 2H<sub>2</sub>O configurations, we also computed the second adsorbate-adsorbate interaction energy using equation (7). This energy is small or negative for all of the 10 promising MOFs listed in Table S3. One example, LEWZET, shows an extremely negative second adsorbate-adsorbate interaction energy of  $-5.48$  eV; this occurs because of significant distortion in the relaxed MOF that occurs due to adsorption of a second water molecule. We note that these effects cannot be explored in existing FF-based searches of MOFs, which assume that the MOF structure is unperturbed by adsorbates. It would be challenging, however, to draw in depth conclusions about selec-

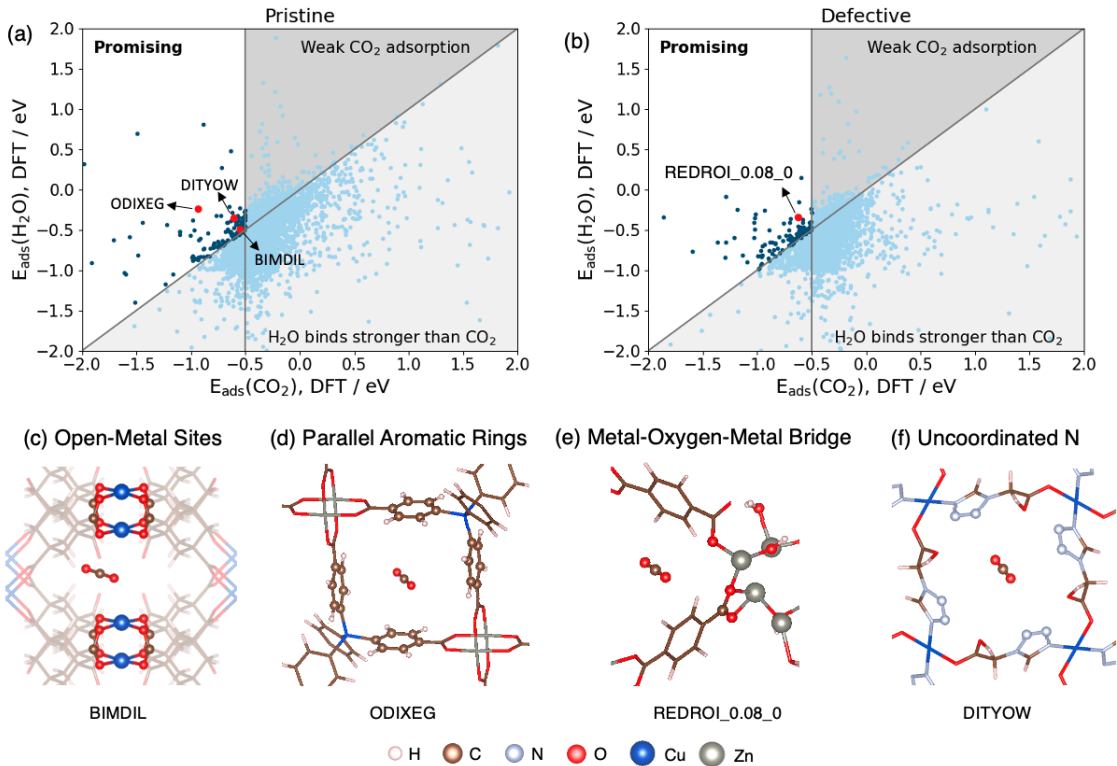


Figure 3: Parity plots showing DFT-calculated  $\text{CO}_2$  and  $\text{H}_2\text{O}$  adsorption energies in (a) pristine and (b) defective MOFs. (c-f) MOF examples with common features of the promising MOFs.

tion of MOFs from a limited number of DFT calculations. The complexities associated with the changes in MOF frameworks during co-adsorption and the challenges with sampling the many possible placements of co-adsorbed states both point to the need to be able to derive FFs or ML models that allow rapid assessment of large numbers of states to provide a thorough description of co-adsorption.

Our results also include the first large collection of adsorbed molecules in defective MOFs relaxed with DFT. The cell volume of most of the MOFs decreased after introducing defects (Fig. S2a). From the 3,628 defective MOFs, we found 107 defective MOFs with  $\text{CO}_2$  adsorption energy greater than water (Fig. 3b). The top 10 defective MOFs, ranked in the same way as the pristine materials, are listed in Table S4. Defects play an important role in the adsorption of water and  $\text{CO}_2$ . For example, pristine TIDLID has adsorption energy of  $-1.10$  eV for  $\text{CO}_2$  and  $-0.52$  eV for  $\text{H}_2\text{O}$  (Fig. S2b), but defective TIDLID was no longer considered promising because the porous structure collapsed and the

PLD was smaller than  $3.3$  Å (Fig. S2c).

The defect concentration was not strongly correlated with the difference in adsorption energies associated with the presence of defects (Fig. S3). The average differences of  $\text{CO}_2$  adsorption energy were nearly zero for all defect concentrations, and adding defects to MOFs resulted in slightly more favorable water adsorption on average. However, the effect of defects on adsorption energies differs greatly from case to case. In Fig. 4a to d, defects in QOV-SOL resulted in more favorable  $\text{H}_2\text{O}$  adsorption and less favorable  $\text{CO}_2$  adsorption, making it no longer a promising candidate for DAC. On the other hand, our calculations with defective MOFs show that the defects in some of these materials can create interesting adsorption environments for DAC. We found multiple cases where pristine MOFs would not be selected based on the criteria defined above, but the defective material is a promising candidate. Fig. 4e to h show one example of POLDUQ. Our observations are broadly consistent with previous experimental and simulation results for



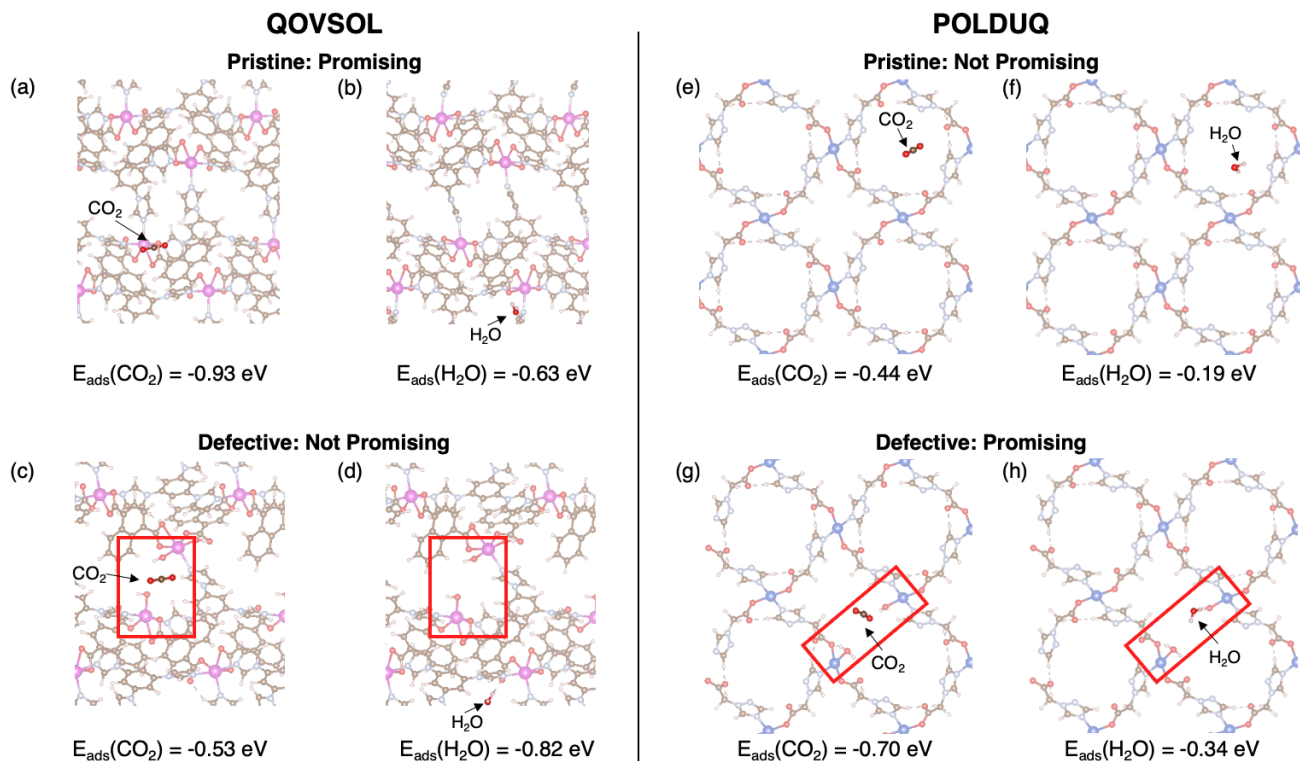


Figure 4: Examples showing different impacts of the defects in MOFs. The defects generated are shown in red squares. Negative impact of defects on DAC (a-d): Defective QOVSOOL with a defect concentration of 0.12 shows less favorable  $\text{CO}_2$  adsorption (a and c) and stronger  $\text{H}_2\text{O}$  adsorption (b and d). Positive impact of defects on DAC (e-g): The  $\text{H}_2\text{O}$  adsorption is slightly more favorable in defective POLDUQ with a defect concentration of 0.06 (f and h), but the  $\text{CO}_2$  adsorption is much stronger at the defect site (e and g).

$\text{CO}_2$  adsorption in UiO-66,<sup>90,91</sup> and enhanced  $\text{CO}_2$  adsorption in Cu-BTC due to water coordinated to OMS.<sup>92</sup> Although defects are capped with water or hydroxyl groups in most cases, it is also possible for defects to create OMSs. The diversity of possibilities illustrates the need for accurate and efficient methods to rapidly explore the many configurations and effects that can exist in defective MOF structures.

It is interesting to ask what motifs or attributes give MOFs adsorption energies that are favorable for DAC. Previous research has suggested several characteristics of good candidates for this application. Boyd *et al.* identified three favorable characteristics: parallel aromatic rings with spacing of approximately 7 Å, metal-oxygen-metal bridges, and open-metal sites.<sup>11</sup> The presence of uncoordinated N atoms has also been proposed as a contributing factor to strong  $\text{CO}_2$  adsorption.<sup>93,94</sup> We exam-

ined these four characteristics (Fig. 3c-f) in our list of promising MOFs: 224 of the 241 of the promising MOFs can be characterized by at least one of these characteristics, confirming their importance. The ODAC23 dataset contains 251 pristine and 267 defective MOFs with an amine functional group. Of these, 7 MOFs (2 pristine and 5 defective) were found to be promising. Structure files of the promising MOFs and the code for promising MOF analysis are available in our open-source repository on GitHub<sup>iii</sup>.

Although the structures in the CoRE MOF set were derived from experiments, it is important to be cautious in concluding that every structure in this dataset is in fact a real material. In developing the CoRE MOF 2019 database, automatic cleaning procedures

<sup>iii</sup>[https://github.com/Open-Catalyst-Project/odac-data/tree/main/promising\\_mof](https://github.com/Open-Catalyst-Project/odac-data/tree/main/promising_mof)

Table 2: 5 pristine MOFs suitable for synthesis on the basis of ODAC23 calculations and manual evaluation of original synthesis reports.

MOF	$E_{\text{ads}}(\text{CO}_2)$	$E_{\text{ads}}(\text{H}_2\text{O})$	PLD	LCD	Metal	Characteristics				Exp. CO <sub>2</sub> Loading (mmol/g)		# of Citations
						OMS	PAR	M-O-M	Uncoordinated N	150 mbar	1 bar	
ODIXEG	-0.94	-0.24	7.80	10.4	Zn	✓	✓					56 <sup>95</sup>
QOVSO	-0.93	-0.63	3.67	6.21	Cd		✓		✓	0.1 (298 K)	0.2 (298 K) <sup>96</sup>	35 <sup>97</sup>
QEFNAQ	-0.57	-0.32	4.72	6.03	Cu	✓	✓			0.4 (293 K)	1.0 (293 K) <sup>98</sup>	272 <sup>99</sup>
FECXES	-0.64	-0.39	6.59	10.83	Cu	✓	✓			1.6 (273 K)	6.3 (273 K) <sup>100</sup>	56 <sup>100</sup>
DITYOW	-0.60	-0.36	4.79	4.86	Cu	✓			✓			52 <sup>101</sup>

Table 3: 5 defective MOFs suitable for synthesis on the basis of ODAC23 calculations and manual evaluation of original synthesis reports.

MOF	Defect conc.	$E_{\text{ads}}(\text{CO}_2)$	$E_{\text{ads}}(\text{H}_2\text{O})$	PLD	LCD	Metal	Characteristics				Exp. CO <sub>2</sub> Loading (mmol/g)		# of Citations
							OMS	PAR	M-O-M	Uncoordinated N	150 mbar	1 bar	
POLDUQ	0.06	-0.70	-0.36	5.09	5.27	Cu	✓			✓			12 <sup>102</sup>
CUGVUW	0.16	-1.14	-0.82	3.41	5.64	Cu		✓		✓			24 <sup>103</sup>
PEPKOL	0.08	-0.62	-0.35	3.46	3.92	Ni		✓					444 <sup>104</sup>
SUJNUH	0.12	-0.93	-0.68	6.62	7.08	Cu		✓			1.3 (195 K)	2.2 (195 K) <sup>105</sup>	77 <sup>105</sup>
LUYHAP	0.16	-0.58	-0.37	8.39	12.35	Cu	✓				3.1 (298 K), <sup>106</sup> 2.5 (296 K), <sup>107</sup> 5.2 (270 K) <sup>107</sup>	158 <sup>106</sup>	

were applied to experimentally reported crystal structures, including the removal of solvent molecules and the resolution of partial occupancies. Although this procedure was generally effective, there are cases where it was too aggressive. We observed linker removal and wrong partial occupancies in a number of the MOFs listed above. Charge-balancing ions were also removed for MOFs denoted ‘charged’ in Table S4. For each MOF listed above, we manually compared the MOF structures retrieved from the CoRE MOF 2019 database and the original publications. From this analysis, we curated a selection of promising MOFs that are completely charge neutral and where the CoRE MOF structure is fully consistent with the original experimental data. On the basis of current DFT data and manual analysis, we expect these to be the most promising MOFs for experimental synthesis and testing. These MOFs are listed in Tables 2 and 3. The tables include the number of times the original synthesis report has been cited, since this has been suggested as a proxy for the ease of synthesis/reuse of a material, and the tables indicate which of the four promising MOF characteristics mentioned above appear in each material. The available CO<sub>2</sub> adsorption isotherms from experimental measurements of these MOFs show relatively strong CO<sub>2</sub> adsorption at low partial pressures,<sup>108</sup> which is consistent with the implications of our calculations.

## Evaluation of the Accuracy of Classical Force Fields

Our large library of DFT calculations allowed us to further investigate the accuracy of existing classical FFs against our DFT calculations. We focus here on the energy of interaction between adsorbed molecules and MOFs, since this is the key calculation underlying previous high throughput assessments of MOFs for CO<sub>2</sub> adsorption. Specifically, we considered a ‘‘standard’’ FF for adsorption in MOFs that combines the UFF4MOF,<sup>109–111</sup> TraPPE,<sup>112</sup> and SPC/E<sup>113</sup> FFs for atoms in the MOF, CO<sub>2</sub>, and H<sub>2</sub>O, respectively. Coulombic interactions were defined using DDEC point charges assigned to MOF atoms from our DFT calculations.<sup>114</sup> Further technical details are provided in the Methods section.

We computed the interaction energy for 51,478 DFT-relaxed MOF + adsorbate systems using the FF and DFT. This is analogous to the energies in the S2EF task. Using interaction energies for this comparison rather than adsorption energies is consistent with previous FF-based studies that assume framework rigidity.<sup>14,28,115,116</sup> The ODAC23 dataset also includes information on MOF deformation associated with the presence of adsorbates, and future work could explore how accurately existing FFs for MOF atoms describe these effects.

The results of our FF calculations and comparisons to DFT interaction energies are shown

in Fig. 5. All structures in this comparison contained only one adsorbate molecule (either  $\text{CO}_2$  or  $\text{H}_2\text{O}$ ), and we omit 226 structures with DFT interaction energies outside the range of  $[-2, 2]$  eV since we suspect these structures are unphysical. We also omit 716 structures with reasonable DFT energies because their FF predictions also fall outside of  $[-2, 2]$  eV. This is done to avoid heavily skewing the subsequent discussion and is revisited at the end of this analysis. Fig. 5a shows that in many cases the difference between the classical FF and DFT is less than 0.25 eV and that many of the DFT results can be described as physisorption. Van der Waals (vdW) interactions dominate within the physisorption regime of  $-0.5 \leq E_{\text{int}}^{\text{DFT}} \leq 0$  eV, and if interaction energies are restricted to this range then the mean absolute error (MAE, or simple *error*) between FF and DFT energies is 0.06 eV. This indicates that the physics-based FFs we tested are quite well adapted to predict the interaction energy when physisorption is dominant.

The results in Fig. 5b–d provide a less promising view of the classical FF. The error between the FF and DFT calculations scales approximately linearly with the DFT energy outside the physisorption regime, showing that the FF predicts a physisorption energy even when DFT indicates that chemisorption is occurring. The minima in these graphs around  $-0.4$  eV again indicate that the FF is only capable of accurately predicting physisorption. In the chemisorption regime from  $-2$  to  $-0.5$  eV, the MAEs for  $\text{CO}_2$  and  $\text{H}_2\text{O}$  are 0.29 eV and 0.39 eV, respectively. Fig. 5b shows the number of points and average error as a function of DFT interaction energy. Although relatively few points outside the physisorption regime exist, the FF interaction energy errors increase drastically with the magnitude of the interaction energy. Many interesting chemistries that are beneficial for DAC occur due to chemisorption (e.g.,  $\text{CO}_2$  binding more strongly than  $\text{H}_2\text{O}$ ). These cases would be missed by a classical FF that is unable to model chemisorption. There are also many instances in which the FF energy prediction is substantially larger than the DFT-calculated energy. We attribute these

to cases involving chemisorption where the adsorbate is close to the framework and therefore returns very large Lennard-Jones energies. That is, the FF exhibits unstable behavior here because very slight changes in geometry cause large spikes in energy predictions.

An additional takeaway from Fig. 5 is that  $\text{H}_2\text{O}$  is significantly more challenging to model than  $\text{CO}_2$ . This is consistent with the fact that physics-based water models are complex and are themselves the subject of a rich body of literature.<sup>117</sup> We found that the error in interaction energy calculations within the  $[-2, 2]$  eV domain involving  $\text{H}_2\text{O}$  (0.19 eV) was more than triple that for  $\text{CO}_2$  (0.05 eV). The vast majority of unstable FF calculations involved  $\text{H}_2\text{O}$  and not  $\text{CO}_2$ . Selecting and implementing an appropriate water model is a non-trivial task that further complicates the use of classical FFs for material screening.

Finally, there are a number of cases where the FFs predict very large interaction energies, with the maximum error being 187.2 eV. These cases typically correspond to dissociative adsorption, where the FF is not an appropriate model. Fig. S5 presents the binned FF errors as a function of the DFT interaction energy for all configurations with a DFT interaction energy in  $[-2, 2]$  eV, irrespective of whether the FF interaction energy falls within this range. Comparison with Fig. 5b shows that the 716 cases with reasonable DFT energies but unreasonable FF energies drastically increase the error, and that catastrophic failures (e.g. errors  $>10$  eV) begin to dominate when the DFT adsorption energies are stronger than 1 eV. The large errors cause the FF MAE for all structures to be quite large at 0.28 eV. If the MAE is calculated only for cases where the FF interaction energy is in the range of  $[-2, 2]$  eV, then the classical FF performs reasonably well with an interaction energy MAE of 0.11 eV across 50,536 calculations. Overall, the results indicate that the FF performs well for physisorption, but fails to capture strong chemical interactions that are likely critical for DAC.

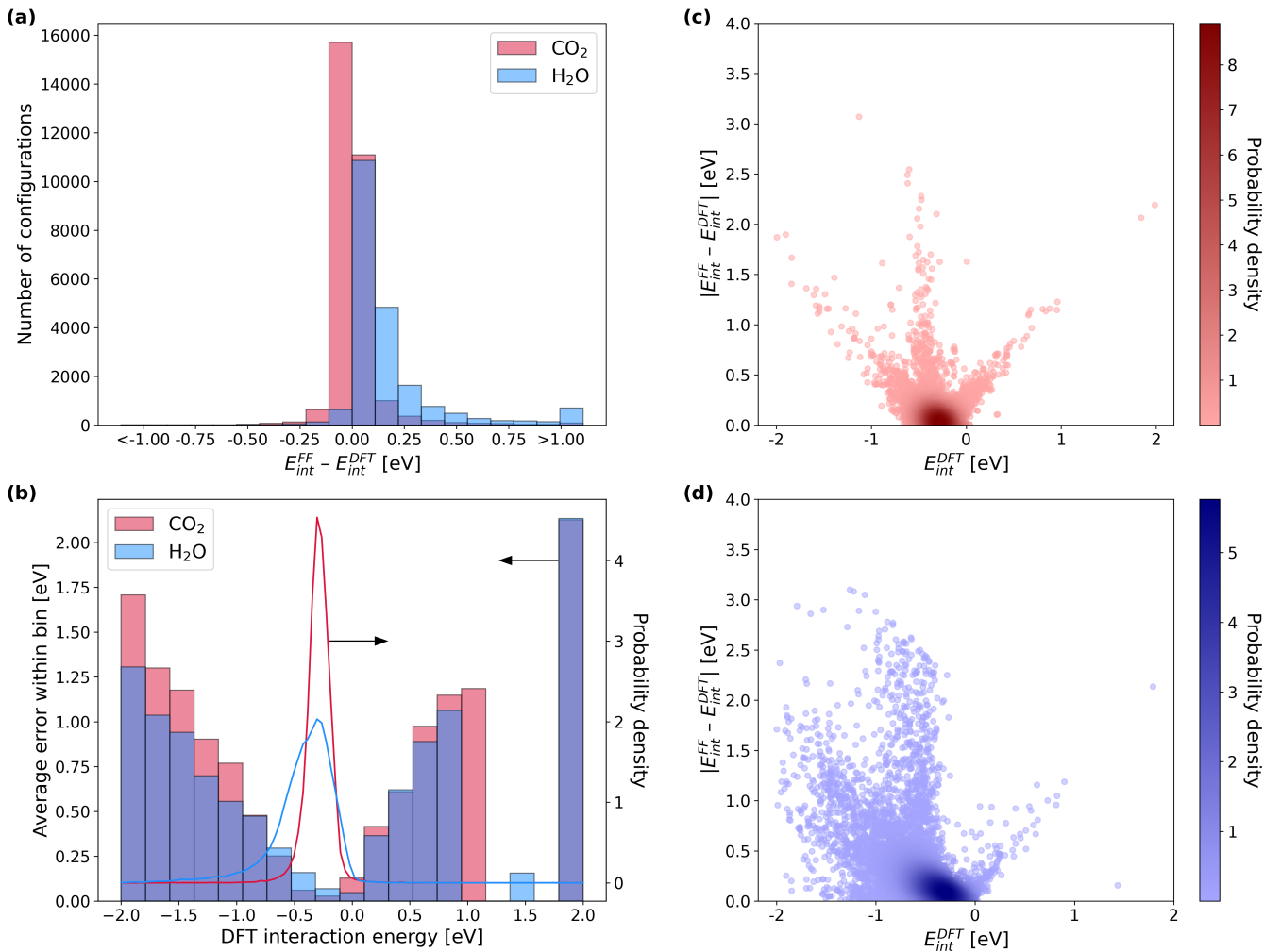


Figure 5: Comparison of adsorbate interaction energies calculated with FFs and DFT. (a) Histogram of energy differences between FF and DFT for 29,644 CO<sub>2</sub> calculations (red) and 20,892 H<sub>2</sub>O calculations (blue). (b) Binned errors and DFT interaction energy distributions split by adsorbate. (c,d) Absolute difference between FF and DFT plotted versus DFT interaction energy for CO<sub>2</sub> and H<sub>2</sub>O, respectively.

## Training and Analysis of Machine Learning Models

We begin by training and benchmarking models for the S2EF task, since it is the most general. We tested six graph neural network (GNN) architectures for this task: SchNet,<sup>118</sup> DimeNet++,<sup>119</sup> PaiNN,<sup>120</sup> GemNet-OC,<sup>121</sup> eSCN,<sup>122</sup> and EquiformerV2.<sup>123</sup> We chose models that performed well on the OC20 and OC22 benchmarks since those datasets and tasks are most similar to ours. These models use GNNs containing equivariant or non-equivariant operations to compute energies and forces. All models were trained to minimize the following

objective function for forces and energies:

$$\mathcal{L} = \lambda_E \sum_i |\hat{E}_i - E_i| + \lambda_F \sum_{i,j} \frac{1}{3N_i} |\hat{F}_{ij} - F_{ij}|^p \quad (2)$$

where the loss coefficients  $\lambda_E$  and  $\lambda_F$  are used to trade-off the force and energy losses.  $E_i$  and  $\hat{E}_i$  are, respectively, the ground truth and predicted energies of system  $i$ , and  $F_{ij}$  and  $\hat{F}_{ij}$  are, respectively, the ground truth and predicted forces for the  $j$ -th atom in system  $i$ . The number of atoms in system  $i$  is denoted by  $N_i$ .  $p$  is the order of the norm – SchNet and DimeNet++ used  $p = 1$ , while the other models used  $p = 2$ .

We used the same model sizes as those used for OC20 (Table S5). To prevent overfitting due to the smaller size of the data set, we adjusted the weight decay for each model. We also slightly adjusted the initial learning rates, batch sizes, learning rate schedules, and the loss coefficients  $\lambda_E$  and  $\lambda_F$ . All error metrics are reported for test sets that were not included in the training and optimization process. Additional information can be found in the Methods section.

The results of all ML models on the S2EF task are presented in Table S6, revealing that GemNet-OC, eSCN, and EquiformerV2 have the best performance. Fig. 6 shows a radar plot comparing these models, indicating that EquiformerV2 (large) achieved the best results for both forces and energies, with a force MAE of 8.20 meV/Å and energy MAE of 0.15 eV on the in-domain test set. The eSCN and GemNet-OC models also performed well, with force MAEs of less than 10 meV/Å and energy MAEs of under 0.17 eV. The models’ relative performance was consistent with their performance on the OC20 and OC22 datasets, suggesting that improvements in model architecture generalize to various materials datasets.

Next, we consider how the models generalize to out-of-domain test sets. The results in Table S6 and Fig. 6 demonstrate that the EquiformerV2 (large) model outperforms the other models on most metrics for all out-of-domain sets. The ML models show only a slight decrease in performance on the test-ood(b) and test-ood(l) sets, suggesting that they generalize well to larger graphs or to new linker chemistry. However, the energy predictions for the test-ood(t) and test-ood(lt) sets are substantially worse than the test-id set, although the force errors are similar to the other test sets. This could be due to errors in long-range vdW interactions for unseen topologies, since this is the main contribution that varies with topology.

We also analyze the performance of the models on the more complex chemical environments of OMSs and defects. OMSs are significant for DAC as they can enable stronger CO<sub>2</sub> adsorption.<sup>46</sup> Classical FFs are known to be less accurate for MOFs with OMSs as they can cause

high polarization in adsorbed molecules.<sup>46,124</sup> Tables S7 and S8 compare GemNet-OC, eSCN, and EquiformerV2 on different subsets of the test-id split. Table S7 shows the performance across pristine MOFs with and without OMSs, and Table S8 compares the performance of the same models on pristine and defective structures. The ML models have similar force MAEs on the OMS and non-OMS sets, as well as the pristine and defective sets. However, the energy MAEs are lower for MOFs without OMSs or defects. This may be due to the stronger and more complex interactions at OMSs, or may be related to the relative abundance of different types of examples within the dataset. Fig. 7a analyzes the binned error for MOFs with and without OMSs, indicating that errors are slightly higher for OMS-containing MOFs in the chemisorption regime, suggesting that the ML models perform slightly worse at predicting the more complex chemical interactions at OMS sites.

A direct comparison between classical FFs and ML models is not feasible because the architecture of the FFs makes it challenging to relax framework atoms. However, we can compare the S2EF adsorption energy errors to the interaction energy errors from FFs to gain insight, since both evaluate the ability to describe interactions between frameworks and adsorbates. We did this with 1,391 relaxed single-adsorbate configurations in the test-id set, which is a subset of the 50,536 structures that excludes all systems used in ML model training. For this reason, energy errors reported in this section may vary slightly from those in the evaluation of the accuracy of classical force fields. The energy MAE for EquiformerV2 (large) for these systems was 0.10 eV, while the MAE for the FF interaction energies on the same structures was 0.49 eV. It is clear that, on average, the best ML models outperform the classical FF models, even when only focusing on relaxed single-adsorbate geometries.

However, a more detailed analysis reveals that the large FF error occurs due to a small number of large failures. The maximum force field error is 67.66 eV, compared to a maximum error of 1.23 eV for the EquiformerV2 (large) model. If

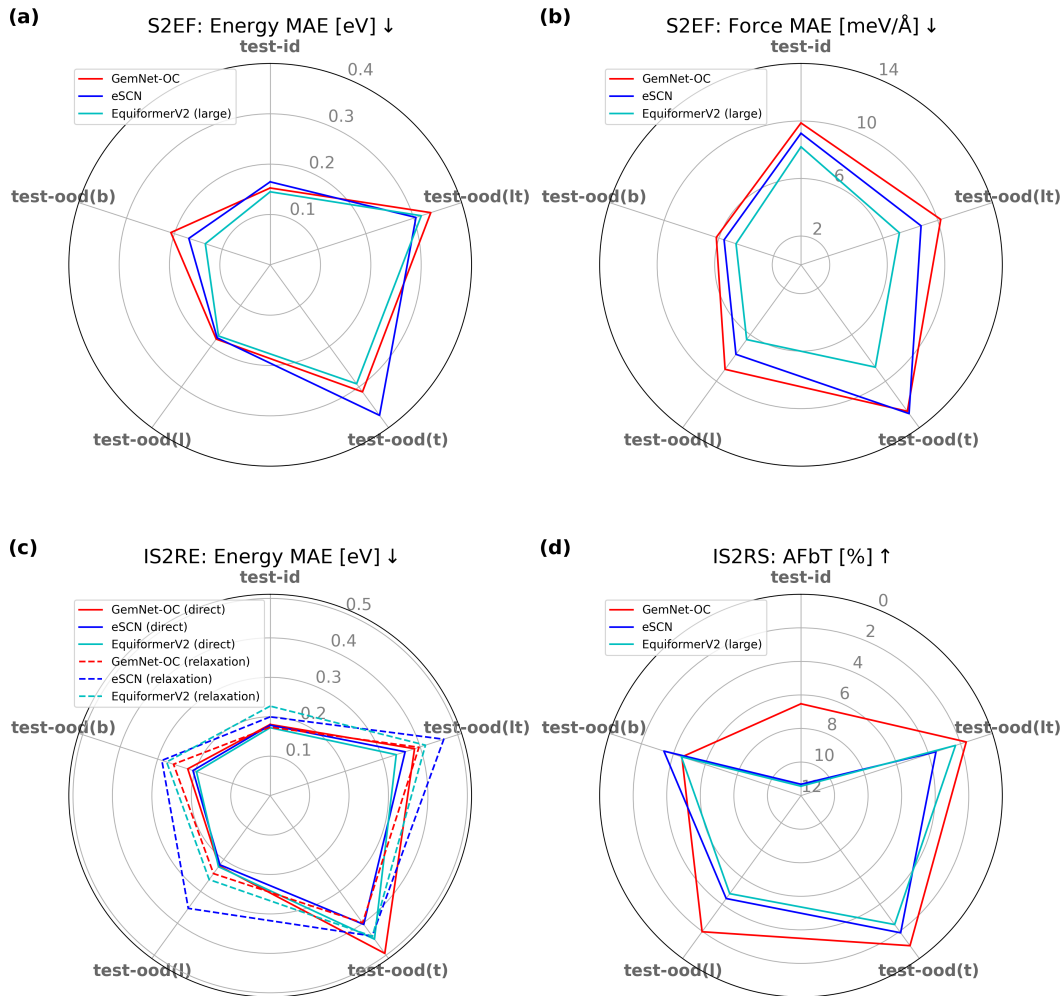


Figure 6: Radar plots for S2EF (a) energy and (b) force MAEs, (c) IS2RE energy MAEs, and (d) IS2RS AFbT for the top three best models – GemNet-OC (red), eSCN (blue), and EquiformerV2 (large, except in (c) where the lighter model is shown) (cyan). Dashed lines correspond to the relaxation approach for IS2RE; all other models are direct predictions. Axes correspond to different in- and out-of-domain test sets, and are aligned so that the best result is closest to the origin of the plot in all cases.

the analysis is restricted to the cases where force fields predict interaction energies in the range of  $[-2, 2]$  eV, the average errors are quite comparable, with MAEs of 0.10 eV for both. In the regime where adsorption energies range from -0.5 to 0 eV and physisorption is expected to be dominant, the FF performance becomes comparable to that of ML, with an MAE of 0.10 eV for the FFs and 0.09 eV for the ML models. A detailed analysis is provided in Fig. 7b, which indicates that ML models exhibit consistently lower errors in the chemisorption regime, in contrast to FF models, which fail for chemisorp-

tion. Given the importance of chemisorption in selective  $\text{CO}_2$  capture at low concentrations, this finding supports the need for ML models for DAC. See Fig. S4 for errors in the repulsive region.

Next, we move to the IS2RE and IS2RS tasks, which evaluate the ability of ML models to directly predict the relaxed adsorption energy (IS2RE) and structure (IS2RS) from an initial guess of framework and adsorbate positions. The IS2RE task only predicts energy and is evaluated with the energy MAE (similar to S2EF) and the “energy within threshold”

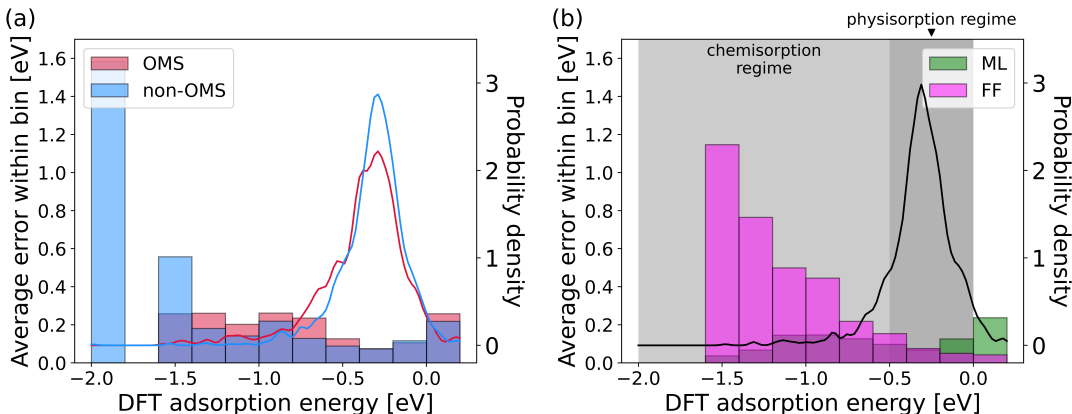


Figure 7: Binned errors and relative density of the number of points (solid lines) as a function of DFT adsorption energy for (a) ML predicted adsorption energies on open metal site (OMS) (red) and non-OMS (blue) and (b) interaction energies predicted by FFs (magenta) and corresponding adsorption energies predicted by ML (green) models. Compared to FFs, ML models are significantly more accurate in the chemisorption regime, and are comparable in the physisorption regime. Positive adsorption energies are omitted from the plot because they are rare and likely unphysical; plots with the full range of adsorption energies are provided in Fig. S4.

(EwT) which evaluates the fraction of predictions within 0.02 eV of the DFT energy. The IS2RE task can be solved by training ML models to directly predict the relaxed adsorption energy from the initial structure (the **direct** method), or by running a structure relaxation with an S2EF model (the **relaxation** method). In the case of the relaxation approach, the task is identical to IS2RS, where the energy of the final structure is used as the IS2RE prediction. However, the metrics used to evaluate the IS2RS task are significantly different, since the goal is to compare structures. The metrics used are the average distance within threshold (ADwT), force below threshold (FbT), and average force below threshold (AFbT), with details provided in the Methods. Evaluating the IS2RS models is quite expensive since it requires performing a DFT single-point for each of the predicted relaxed structures. Therefore, we only evaluated the best 4 models (GemNet-OC, eSCN, EquiformerV2, and EquiformerV2 (large)) and only computed DFT single-point energies on 500 randomly selected structures from each test split.

For the IS2RE task, any S2EF model can be used for the indirect approach, so we evaluated all six S2EF models from this work using the model to perform structure relaxations

with each model. The resulting structures are also used for the IS2RS task. In addition, we selected the best three models – GemNet-OC, SCN, and EquiformerV2 – and retrained them for the direct approach, with settings identical to the corresponding S2EF models unless otherwise noted.

Fig. 6 and Table S9 show the results for the IS2RE task on each of the test splits. On the test-id set, the direct methods obtain an energy MAE around 0.18 eV and an EwT of over 10%. The relaxation approach with older S2EF models like SchNet, DimeNet++, and PaiNN perform worse than direct methods, while newer methods such as GemNet-OC, eSCN, EquiformerV2, and EquiformerV2 (large) are marginally better than direct approaches. Similar to the S2EF task, we find that the performance of the ML models degrades marginally on the test-ood(b) or test-ood(l) datasets, while they degrade significantly on the test-ood(t) and test-ood(lt) datasets. This is true for both direct and relaxation-based approaches.

Fig. 6 and Table S10 show the IS2RS results on each test split. The ADwT results are reasonably high for the test-id and test-ood(b) sets but degrade significantly for test-ood(l) and test-ood(t) sets. However, the results

on the DFT-based metrics (FbT and AFbT) indicate that the models achieve relaxed structures consistent with what would be obtained from DFT  $< 1\%$  of the time in all cases (and  $0\%$  in many cases). This inconsistency between ADwT and (A)FbT has also been observed for OC20<sup>75</sup> and indicates that the models need significant improvement to achieve the level of accuracy needed to replace DFT for the prediction of relaxed structures. However, the fact that the models are able to predict the energies of relaxed structures with reasonable accuracy in the IS2RE task is an encouraging sign, since the state of the art for high throughput MOF screening with force field is to assume that the structures are rigid. This assumption becomes particularly questionable in the case of defective MOFs or strong adsorption, indicating the need for models capable of accounting for relaxation effects.

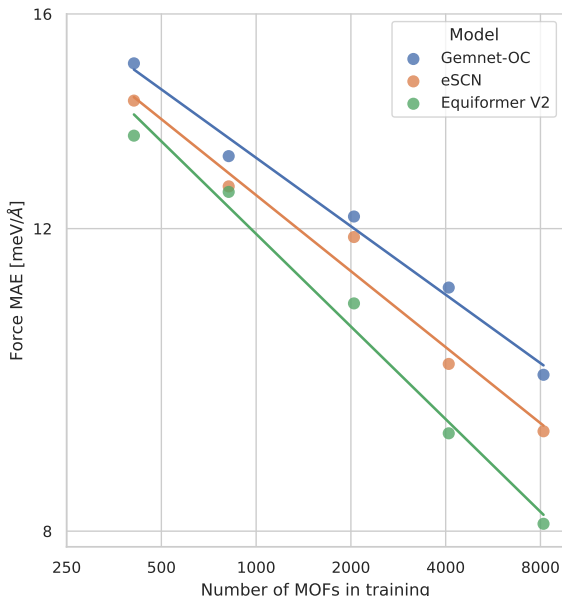


Figure 8: Force MAE on the test-id set for the top 3 S2EF models when trained on different amounts of training data. The lines show scaling laws obtained by fitting a line between log of the force MAE and log of the number of training MOFs for each model.

It is clear that the ML models presented here demonstrate significant promise compared to the standard classical FF models. However, there are also obvious deficiencies. One ad-

vantage of ML models is that they tend to improve with more data. In particular, scaling laws for deep learning models relate model performance to a parameter like the number of model parameters or size of the training dataset. Scaling laws have helped to choose the optimal model and training parameters in several domains.<sup>125–127</sup> Fig. 8 shows the scaling laws for the ODAC23 dataset size, comparing the force MAEs of different models as a function of the number of MOFs in the training data. Consistent with previous work in other domains, we observe a power-law relationship between force MAE and the number of MOFs. This implies that we can continue to improve the performance of these models by including more training data. It is also interesting to note that equivariant models like EquiformerV2 and eSCN have better scaling properties than GemNet-OC, matching the findings of Batzner *et al.*<sup>128</sup> This indicates that the use of more sophisticated model architectures is a promising route forward.

Based on these scaling laws, a much larger number of MOFs would be required to achieve force MAEs of  $3 \text{ meV}/\text{\AA}$  (approaching the numerical error of DFT). An alternative strategy common in deep learning is to leverage similar datasets. This has proven useful in the Open Catalyst Project models,<sup>129</sup> and we plan to explore this approach in future work. Another possible strategy is to develop model architectures that are tailored for the DAC application. In particular, the strong performance of FFs in the weak-binding regime suggests that incorporating information on vdW interactions into the model<sup>130</sup> or  $\Delta$ -ML<sup>131</sup> models may be promising strategies. Ultimately, we expect that improved model architectures, advanced transfer learning, and joint training techniques may provide a route to leveraging physical knowledge and other large atomistic datasets to improve performance on ODAC23, although we leave this as future work.<sup>132,133</sup>



# Impact and Future Outlook

The results of this study provide the most comprehensive DFT dataset of CO<sub>2</sub> and H<sub>2</sub>O adsorption in MOFs available. Analysis of the resulting DFT calculations has shown that, contrary to the findings from FF-based studies, there are numerous MOF-based adsorption sites with strong and selective CO<sub>2</sub> adsorption. A direct comparison of the DFT results to classical FFs provides the most comprehensive perspective to date on the accuracy of FFs. The results reveal that the FFs work well in cases where vdW interactions dominate but fail when stronger bonding is involved. These findings demonstrate that high-throughput screening with methods capable of treating chemisorption and framework distortion will be required to identify MOFs that can strongly and selectively bind CO<sub>2</sub> under humid conditions.

In addition, the work provides a benchmark for state-of-the-art ML models for CO<sub>2</sub> and H<sub>2</sub>O adsorption in MOFs. The results indicate that the best performing GNN models, such as EquiformerV2, are capable of predicting adsorption energies with average errors of  $\sim 0.15 - 0.3$  eV, and forces with errors of  $\sim 5-10$  meV/Å. Comparison with a classical FF shows that these ML models are more accurate outside the regime of vdW interactions. This, coupled with the importance of strong binding in identifying selective CO<sub>2</sub> adsorption sites, suggests that these ML models have the potential to replace classical FFs as the standard approach in high-throughput MOF screening for DAC and other applications in separations and catalysis.

Moving forward, it will be important to critically evaluate and improve ML models and associated datasets so that they can be applied to other steps in the computational sorbent selection process. For example, grand canonical Monte Carlo simulations are critical for predicting adsorption isotherms. The models here are untested for this task since they have not seen configurations with higher molecular loadings. Testing and improving the models will facilitate calculation of full single and multicomponent isotherms with accuracies that approach DFT.

This is especially critical for the case of bicomponent CO<sub>2</sub>/H<sub>2</sub>O isotherms that are needed to predict the behavior of MOF materials in DAC process models. The complex mixture of vdW, hydrogen, and covalent bonding in H<sub>2</sub>O makes it difficult to accurately predict these bicomponent isotherms with existing methods, but the ML models presented here provide a promising foundation for future developments.

## Methods

### ODAC23 Dataset Generation

A workflow diagram with details on the dataset generation workflow is provided in Fig. S6, and more details are provided in the sub-sections below.

#### Structure relaxations

DFT relaxations used the PBE exchange–correlation functional<sup>81</sup> with a D3 dispersion correction<sup>82</sup> including Becke-Johnson damping and with spin polarization.<sup>83</sup> Relaxations were performed with conjugate gradient methods with a step size of 0.01, and Gaussian smearing was used with a width of 0.2 eV. A plane wave cutoff energy of 600 eV to minimize effects of Pulay stress and a precision of  $10^{-5}$  eV were used. All simulations were performed in the Vienna Ab Initio Simulation Package (VASP) v5 software with a 1x1x1 k-point grid.<sup>134</sup>

We relaxed all 8,803 CoRE MOF pristine structures using DFT as described above before generating defective structures and placing adsorbate molecules, and a total of 5,079 MOFs converged. DFT convergence failures are due to a variety of issues. For example, Chen and Manz identified several failure modes in CoRE MOF input files beyond overlapping atoms (3.5% of all screened structures), including isolated atoms (7.8%), misbonded hydrogens (1.3%), and over/underbonded carbons (15.3%).<sup>79</sup> Examples of VASP convergence issues were large systems that took too long or ran out of memory ( $\sim 10\%$  of screened structures) and numerical errors pertaining to

Hamiltonian diagonalization. We noticed several converged structures with very high initial formation energies ( $>3$  eV/atom). All initial inputs of converged structures were thus screened for overlapping atoms resulting from imperfect solvent removal processes and partial occupancies in the CoRE work. We used the published list of effective atomic radii by Chen and Manz for atom typing; a structure failed if any atom pairs were less than half the sum of their respective atomic radii apart.<sup>79</sup> In total, 161 structures failed and were excluded from further analysis due to overlapping atoms and unphysically large initial formation energies.

### Defective MOF generation

We expanded the pristine set of MOFs from CoRE MOF by introducing missing linker defects using the methods introduced recently by Yu *et al.*<sup>85</sup> This approach requires identification of the linker and nodes in each MOF, a task completed using the algorithm MOFid developed by Bucior *et al.*<sup>135</sup> Out of 5,079 pristine MOFs that converged in our DFT calculations, we successfully identified the nodes and linkers of 4,780 MOFs. In each MOF we created structures with different defect concentrations from 0.01 to 0.16, where the defect concentration is defined as the number of removed linkers divided by the total number of linkers. For MOFs that have multiple types of linkers, we generated corresponding defective structures by removing one kind of linker at a time. OMSs were capped using either a water molecule if the removed linker is charge neutral or hydroxyl(s) if the removed linker was charged to create structures that have no overall charge. In total, 16,358 distinct structures were generated and relaxed by DFT, and 6,340 of them converged. We only kept the relaxed structures with PLD  $> 3.3$  Å, and the final set of defective MOFs contained 3,470 frameworks.

### Adsorbate placement

In each relaxed MOF (either pristine or defective) structure, we placed an adsorbate(s) using non-bonded pairwise interactions defined

by one of the classical FFs by the RASPA 2.0 package.<sup>33</sup> FF parameters for framework atoms and adsorbates ( $\text{CO}_2$  and  $\text{H}_2\text{O}$ ) were defined by the United Force Field (UFF)<sup>109</sup> and TraPPE-United Atom FF,<sup>136</sup> respectively. Specifically, we adopted the rigid TIP5P model for  $\text{H}_2\text{O}$  molecules.<sup>137,138</sup> The Lorentz-Berthelot mixing rules and a tail correction with a cutoff radius of 14 Å were used to define the Lennard-Jones interactions between MOFs and adsorbates. Coulombic interactions were considered when partial charges of the framework atoms were available by the DDEC method. We collected configurations of [MOF+ $\text{CO}_2$ ] or [MOF+ $\text{H}_2\text{O}$ ] from every 10,000 Monte Carlo cycles with the same translation, rotation, and reinsertion probabilities. We took two approaches to ensure that structures do not have duplicated positions and exhibit diversity in structures: (i) energy matching and (ii) random sampling. The energy matching approach notes that different non-bonded interaction energies will correspond to different configurations. Starting from the minimum observed energy, we sampled configurations in 5 kJ/mol intervals until the non-bonded interaction energy reached a threshold ( $-15$  kJ/mol and  $-5$  kJ/mol for  $\text{CO}_2$  and  $\text{H}_2\text{O}$ , respectively). If the minimum energy was greater than the threshold, we included only the configuration with the minimum energy. No configuration was added for cases where the minimum energy was  $> 0$  kJ/mol. This resulted in having 0-9 adsorbate placements for each MOF structure, leading to a diverse collection of more than 10,000 MOF+adsorbate configurations per adsorbate by the energy matching approach. For random sampling, we randomly chose 2 configurations from the collection of 10,000 cycles and added these configurations to the set selected from energy matching, leading to more than 16,000 MOF+adsorbate configurations per adsorbate by the random sampling approach. Several MOF structures were further excluded from the dataset because their pore size shrunk during the relaxation, making it impossible for RASPA to place an adsorbate in their pores. We manually added 158 converged [MOF+ $\text{H}_2\text{O}$ ] configurations to position water molecules closer

to OMSs. This was done for MOF structures where a CO<sub>2</sub> molecule was near OMSs without nearby water or when they were identified as promising but with fewer than 4 H<sub>2</sub>O placements.

For co-adsorption cases, we used a similar strategy to obtain configurations. Co-adsorption studies include the following examples: [1CO<sub>2</sub>+1H<sub>2</sub>O] and [1CO<sub>2</sub>+2H<sub>2</sub>O]. In each study, we inserted all of the participating molecules into each empty MOF structure. Since we are interested in the behavior of CO<sub>2</sub> in the presence of water, we discarded configurations where the distance between the centers-of-mass for any pair of adsorbate molecules was greater than 5 Å. For MOF structures whose primitive cells were too small to place multiple adsorbates in the pores, the primitive cell was repeated to form a bigger supercell. Whether a supercell was used to save the configuration can be found on GitHub.<sup>iv</sup> Both energy matching and random sampling strategies were applied to multi-adsorbate configurations. The energy threshold was set to be -5 kJ/mol for all molecule combinations in case of energy matching approach.

After placing adsorbates, we perform DFT structure relaxations on each adsorbate-MOF configuration. We used the same DFT settings as the MOF relaxations but with fixed unit cell parameters.

### Out-of-Domain MOF selection

The ODAC23 dataset contains four out-of-domain (OOD) test sets in addition to the in-domain test set to evaluate the ability of ML models trained on the ODAC23 dataset to new topologies, new linker chemistries, and to larger MOFs.

The **test-ood (big)** or test-ood(b) test split only contains MOFs with over 500 atoms in their unit cells. Testing on this set allows us to assess how well our models generalize to larger MOFs than those contained in the training set.

The other three OOD test sets were designed to study how our ML models generalize to new

chemistries and topologies not present in Core-MOF. To create these splits, we sampled structures from the “ultrastable MOF database” developed by Nandy *et al.*<sup>76</sup> To create our OOD test sets, we selected the ultrastable MOFs with less than 500 atoms, and contained either novel linkers or topologies not present in the rest of our dataset. This allowed us to create three OOD test sets: the **test-ood (linker)** set contains novel linkers but known topologies, the **test-ood (topology)** set contains novel topologies but known linkers, and the **test-ood (linker & topology)** set contains both novel linkers and novel topologies. We abbreviate these three sets as test-ood(l), test-ood(t), and test-ood(lt) respectively. We used the MOFid library<sup>135</sup> to identify the organic linkers and topologies.

We believe that the inclusion of these OOD sets, which are biased to a property not related to the DAC application, provides a useful test of the generalizability of our trained ML models.

### Energy Definitions

We defined three energy definitions for analysis of our work. Throughout this section,  $E_A^B$  denotes the total energy of a system of interest  $A$  calculated by a method  $B$ . If not specifically noted,  $B$  defaults to DFT. Energies are a function of atomic coordinates ( $C$ ) either from DFT relaxation ( $r_C^{\text{relax}}$ ) or from a single-point DFT calculation ( $r_C^{\text{single}}$ ).

**Adsorption energy** The adsorption energy can be defined as:

$$E_{\text{ads}} = E_{\text{system}}(r_{\text{system}}^{\text{relax}}) - E_{\text{MOF}}(r_{\text{MOF}}^{\text{relax}}) - n_{\text{CO}_2} E_{\text{CO}_2}(r_{\text{CO}_2}^{\text{relax}}) - n_{\text{H}_2\text{O}} E_{\text{H}_2\text{O}}(r_{\text{H}_2\text{O}}^{\text{relax}}) \quad (3)$$

where  $E_{\text{system}}$  is the DFT energy of the MOF + adsorbate system,  $E_{\text{MOF}}$  is the reference DFT energy of the relaxed standalone MOF,  $n_{\text{CO}_2}$  and  $n_{\text{H}_2\text{O}}$  denote the number of CO<sub>2</sub> and H<sub>2</sub>O molecules in the system respectively, and  $E_{\text{CO}_2}$  and  $E_{\text{H}_2\text{O}}$  are the gas phase energies of the corresponding molecules.

In equation (3), the structure of the MOF in the system and the standalone MOF are from

<sup>iv</sup>[https://github.com/Open-Catalyst-Project/odac-data/tree/main/supercell\\_info.csv](https://github.com/Open-Catalyst-Project/odac-data/tree/main/supercell_info.csv)

separate DFT relaxations. When a supercell was created during adsorbate placement, the reference energy  $E_{\text{MOF}}$  was computed by performing an additional DFT relaxation on the supercell without the adsorbate.

The inclusion of adsorbate molecules during relaxation broke framework symmetry and resulted in lower energy empty MOF configurations in a small number of cases. We conducted a second round of relaxations on these empty MOFs and successfully found lower energy states for 690 pristine and 625 defective MOFs. These lower energy states were used as the reference energy for all adsorption energy calculations. We removed all configurations where the adsorption energy was found to be  $< -2$  eV per adsorbate.

We also define  $\tilde{E}_{\text{ads}}$  for which we obtained the total energy of the current MOF + adsorbate configuration instead of seeking its relaxed state. This can be expressed as:

$$\begin{aligned} \tilde{E}_{\text{ads}} = & E_{\text{system}}(r_{\text{system}}^{\text{single}}) - E_{\text{MOF}}(r_{\text{MOF}}^{\text{relax}}) \\ & - n_{\text{CO}_2} E_{\text{CO}_2}(r_{\text{CO}_2}^{\text{relax}}) - n_{\text{H}_2\text{O}} E_{\text{H}_2\text{O}}(r_{\text{H}_2\text{O}}^{\text{relax}}) \end{aligned} \quad (4)$$

$\tilde{E}_{\text{ads}}$  indicates how far the current state of a MOF + adsorbate system is from its reference state and is used as one of the main targets in our ML studies. In the case that  $\tilde{E}_{\text{ads}}$  is computed from the single-point DFT calculation of a relaxed structure (i.e.  $r_{\text{system}}^{\text{single}} = r_{\text{system}}^{\text{relax}}$ ) it is equivalent to  $E_{\text{ads}}$ .

**Interaction energy** The interaction energy is defined as:

$$\begin{aligned} E_{\text{int}} = & E_{\text{system}}(r_{\text{system}}^{\text{relax}}) - E_{\text{MOF}}(r_{\text{system}}^{\text{relax}}) \\ & - n_{\text{CO}_2} E_{\text{CO}_2}(r_{\text{system}}^{\text{relax}}) - n_{\text{H}_2\text{O}} E_{\text{H}_2\text{O}}(r_{\text{system}}^{\text{relax}}) \end{aligned} \quad (5)$$

where  $E_{\text{int}}$  was calculated either by DFT ( $E_{\text{int}}^{\text{DFT}}$ ) or the classical FF ( $E_{\text{int}}^{\text{FF}}$ ).

Interaction energies calculations were performed only on the relaxed MOF + adsorbate configurations using single-point DFT. For simplicity, interaction energies were computed only in single adsorption cases, thus  $n_{\text{CO}_2} + n_{\text{H}_2\text{O}} = 1$  in equation (5).

### Adsorbate-adsorbate interaction energy

The adsorbate-adsorbate interaction energy quantifies interactions between adsorbates in co-adsorption cases and is defined as:

$$\begin{aligned} E_{\text{inter\_mol}}^{\text{1st}} = & E_{\text{ads}}(\text{CO}_2 + \text{H}_2\text{O}) \\ & - E_{\text{ads}}(\text{CO}_2) - E_{\text{ads}}(\text{H}_2\text{O}) \end{aligned} \quad (6)$$

$$\begin{aligned} E_{\text{inter\_mol}}^{\text{2nd}} = & E_{\text{ads}}(\text{CO}_2 + 2\text{H}_2\text{O}) \\ & - E_{\text{ads}}(\text{CO}_2 + \text{H}_2\text{O}) - E_{\text{ads}}(\text{H}_2\text{O}) \end{aligned} \quad (7)$$

where the number of each adsorbate is shown in parentheses. The first adsorbate-adsorbate interaction energy ( $E_{\text{inter\_mol}}^{\text{1st}}$ ) shows the adsorbate-adsorbate interactions between  $\text{CO}_2$  and  $\text{H}_2\text{O}$  and the second adsorbate-adsorbate interaction energy ( $E_{\text{inter\_mol}}^{\text{2nd}}$ ) shows the adsorbate-adsorbate interactions induced by introducing a second  $\text{H}_2\text{O}$  molecule.

## Evaluation Metrics

For all machine learning models we use the same evaluation metrics used for OC20. We briefly describe the metrics used for each task in this section, but refer the reader to the OC20 paper<sup>75</sup> for more details.

### Structure to Total Energy and Forces (S2EF)

The S2EF task is evaluated on the accuracy of force and adsorption energy predictions through the following metrics. For these metrics  $E \equiv \tilde{E}_{\text{ads}}$  computed by equation 4.

- Energy MAE: Mean absolute error between the predicted energy and the ground truth energy :

$$EMAE = \frac{1}{N} \sum_i |\hat{E}_i - E_i|, \quad (8)$$

where  $E_i$  and  $\hat{E}_i$  are the ground truth and predicted energies of system  $i$  and  $N$  is the total number of systems.

- Force MAE: Mean absolute error between

predicted and ground truth DFT forces:

$$FMAE = \frac{1}{N} \sum_i \frac{1}{N_i} \sum_j \|\hat{F}_{ij} - F_{ij}\|_1, \quad (9)$$

where  $F_{ij}$  and  $\hat{F}_{ij}$  are the predicted and ground truth forces on the  $j$ -th atom of system  $i$  and  $N_i$  is the number of atoms in system  $i$ .

- Force Cos: Cosine similarity between the predicted and ground truth forces.
- Energy and forces within threshold (EFwT): The fraction of energies and forces that are respectively within 0.02 eV and 0.03 eV/Å of the ground truth DFT values.

**Initial Structure to Relaxed Energy (IS2RE)** : The IS2RE task is evaluated on the accuracy of relaxed energy predictions using the following metrics. For these metrics  $E \equiv E_{ads}$  computed by equation 3.

- Energy MAE: Mean absolute error between predicted energy and the ground truth DFT energy of the relaxed state.
- Energy within Threshold (EwT): The fraction of energies within 0.02 eV of the DFT relaxed energy.

**Initial Structure to Relaxed Structure (IS2RS)** : The IS2RS task is evaluated on whether the predicted relaxed structure is close to a local minimum in the energy landscape using the following metrics.

- Average Distance within Threshold (ADwT): Distance within Threshold (DwT) is the percentage of structures with an atom position MAE below a threshold  $\beta$ . ADwT averages DwT across thresholds ranging from  $\beta_0 = 0.01$  Å to  $\beta_1 = 0.5$  Å in increments of 0.001 Å.
- Force below Threshold (FbT): Percentage of relaxed structures with maximum DFT

calculated per-atom force magnitudes below a threshold of  $\alpha = 50$  meV/Å. This is only computed for structures that satisfy the DwT criterion with  $\beta = 0.5$  Å.

- Average Force below Threshold (AFbT): FbT averaged over a range of thresholds:  $\alpha_0 = 10$  meV/Å to  $\alpha_1 = 400$  meV/Å in increments of 1 meV/Å.

As the systems in ODAC23 do not contain any fixed atoms, per-atom metrics like Force MAE, ADwT, FbT and AFbT are computed over all atoms. Note that a new single point DFT calculation is required to evaluate FbT and AFbT on a given data point.

## Classical Force Fields

All classical FF calculations in this work used the readily available MOF extension to the ubiquitous UFF force field (UFF4MOF)<sup>110,111</sup> in the Large-scale Atomic/Molecular Massively Parallel Simulator (LAMMPS).<sup>36</sup> Topology files were generated using LAMMPS Interface.<sup>139</sup> CO<sub>2</sub> and H<sub>2</sub>O molecules were described using the TraPPE<sup>112</sup> and SPC/E<sup>113</sup> models, respectively. The SPC/E model was chosen to avoid challenges related to the geometry of massless sites in newer models such as TIP5P,<sup>137</sup> which was used for adsorbate placement but can be cumbersome to place in high-throughput FF calculations. Electrostatic interactions were described using DDEC framework point charges provided as part of the ODAC23 dataset,<sup>114</sup> and long-range interactions were computed using an Ewald summation with a force tolerance of 10<sup>-5</sup> kcal/mol/Å. The cutoff for all pairwise interactions was 12.5 Å. Periodic boundary conditions were applied in all calculations, and tail corrections were not applied. Code for FF calculations is available in our open-source repository on GitHub<sup>v</sup>.

## ML Models

Various ML FF models have been proposed for molecular and material tasks over the last

<sup>v</sup>[https://github.com/Open-Catalyst-Project/odac-data/tree/main/force\\_field](https://github.com/Open-Catalyst-Project/odac-data/tree/main/force_field)

few years.<sup>118,120–123,140–142</sup> Here, we benchmark a subset of the state-of-the-art models on our tasks. All of our models were implemented using PyTorch<sup>143</sup> and the code is available in our open-source repository on GitHub<sup>vi</sup>.

For S2EF, we trained SchNet,<sup>118</sup> DimeNet++,<sup>119</sup> GemNet-OC,<sup>142</sup> PaiNN,<sup>140</sup> eSCN,<sup>122</sup> and EquiformerV2<sup>123</sup> models. We trained 2 versions of the EquiformerV2 model – a small 31M parameter model and a large 153M parameter model. The list of models used is summarized in Table S5. Edges were computed on-the-fly using a nearest-neighbor search with a cutoff of 8 Å and a maximum of 50 neighbors for SchNet, DimeNet++ and PaiNN, and a maximum of 20 neighbors for eSCN and EquiformerV2. GemNet-OC uses different cutoffs for different types of interaction triplets and quadruplets. These S2EF models can then be used to run machine learning relaxations to solve the IS2RE and IS2RS task. We benchmarked the top performing S2EF models – GemNet-OC, eSCN and EquiformerV2 – to run these ML relaxations using the L-BFGS optimizer for 125 steps or until the magnitude of the predicted forces on each atom was less than 0.05 eV/Å. IS2RE can also be solved by directly predicting the energy from the initial system, which we call *direct IS2RE prediction*. We trained GemNet-OC, eSCN and EquiformerV2 models on the direct IS2RE task.

**Acknowledgement** The authors acknowledge Larry Zitnick (Meta), Joe Spisak (Meta), and Julius Kusuma (Meta) for helpful discussions about the project, Muhammed Shuaibi (Meta) for feedback on dataset construction, and Kyle Michel (Meta) for his help with the compute infrastructure necessary for running DFT calculations.

**Notice of Copyright** : This manuscript has been authored by UT-Battelle, LLC, under contract DE-AC05-00OR22725 with the US Department of Energy (DOE). The publisher acknowledges the US government license to provide public access under the DOE Public Access Plan (<http://energy.gov/downloads/doe>

public-access-plan)

## References

- (1) Cheng, W.; Dan, L.; Deng, X.; Feng, J.; Wang, Y.; Peng, J.; Tian, J.; Qi, W.; Liu, Z.; Zheng, X.; Zhou, D.; Jiang, S.; Zhao, H.; Wang, X. Global monthly gridded atmospheric carbon dioxide concentrations under the historical and future scenarios. *Scientific Data* **2022**, *9*.
- (2) Sood, A.; Vyas, S. Carbon Capture and Sequestration- A Review. *IOP Conference Series: Earth and Environmental Science* **2017**, *83*, 012024.
- (3) Sanz-Pérez, E. S.; Murdock, C. R.; Didas, S. A.; Jones, C. W. Direct Capture of CO<sub>2</sub> from Ambient Air. *Chemical Reviews* **2016**, *116*, 11840–11876.
- (4) Realff, M. J.; Eisenberger, P. Flawed analysis of the possibility of air capture. *Proceedings of the National Academy of Sciences* **2012**, *109*.
- (5) Tiainen, T.; Mannisto, J. K.; Tenhu, H.; Hietala, S. CO<sub>2</sub> Capture and Low-Temperature Release by Poly(aminoethyl methacrylate) and Derivatives. *Langmuir* **2021**, *38*, 5197–5208.
- (6) Sholl, D. S.; Lively, R. P. Seven chemical separations to change the world. *Nature* **2016**, *532*, 435–437.
- (7) Farha, O. K.; Özgür Yazaydın, A.; Eryazici, I.; Malliakas, C. D.; Hauser, B. G.; Kanatzidis, M. G.; Nguyen, S. T.; Snurr, R. Q.; Hupp, J. T. De novo synthesis of a metal-organic framework material featuring ultrahigh surface area and gas storage capacities. *Nature Chemistry* **2010**, *2*, 944–948.
- (8) Park, J.; Landa, H. O. R.; Kawajiri, Y.; Realff, M. J.; Lively, R. P.; Sholl, D. S. How Well Do Approximate

<sup>vi</sup><https://github.com/Open-Catalyst-Project/ocp>

- Models of Adsorption-Based CO<sub>2</sub> Capture Processes Predict Results of Detailed Process Models? *Ind. Eng. Chem. Res.* **2020**, *59*, 7097–7108.
- (9) Kim, S. H.; Landa, H. O. R.; Ravutla, S.; Realff, M. J.; Boukouvala, F. Data-driven simultaneous process optimization and adsorbent selection for vacuum pressure swing adsorption. *Chem. Eng. Research and Design* **2022**, *118*, 1013–1028.
- (10) Leonizo, G.; Shah, N. Innovative Process Integrating Air Source Heat Pumps and Direct Air Capture Processes. *Ind. Eng. Chem. Res.* **2022**, *61*, 13221–13230.
- (11) Boyd, P. G. et al. Data-driven design of metal–organic frameworks for wet flue gas CO<sub>2</sub> capture. *Nature* **2019**, *576*, 253–256.
- (12) Findley, J. M.; Sholl, D. S. Computational Screening of MOFs and Zeolites for Direct Air Capture of Carbon Dioxide under Humid Conditions. *The Journal of Physical Chemistry C* **2021**, *125*, 24630–24639.
- (13) Chen, C.; Yu, Z.; Sholl, D. S.; Walton, K. S. Effect of Loading on the Water Stability of the Metal-Organic Framework DMOF-1 [Zn(bdc)(dabco)<sub>0.5</sub>]. *J. Phys. Chem. Lett.* **2022**, *13*, 4891–4896.
- (14) You, W.; Liu, Y.; Howe, J. D.; Sholl, D. S. Competitive Binding of Ethylene, Water, and Carbon Monoxide in Metal Organic Framework Materials with Open Cu Sites. *J. Phys. Chem. C* **2018**, *122*, 8960–8966.
- (15) Wilmer, C. E.; Farha, O. K.; Bae, Y.-S.; Hupp, J. T.; Snurr, R. Q. Structure–property relationships of porous materials for carbon dioxide separation and capture. *Energy Environ. Sci.* **2012**, *5*, 9849–9856.
- (16) Daglar, H.; Keskin, S. Recent advances, opportunities, and challenges in high-throughput computational screening of MOFs for gas separations. *Coord. Chem. Rev.* **2020**, *422*, 213470.
- (17) Lin, L.-C.; Berger, A. H.; Martin, R. L.; Kim, J.; Swisher, J. A.; Jariwala, K.; Rycroft, C. H.; Bhowan, A. S.; Deem, M. W.; Haranczyk, M.; Smit, B. In silico screening of carbon-capture materials. *Nature Materials* **2012**, *11*, 633–641.
- (18) Kim, J.; Abouelnasr, M.; Lin, L.-C.; Smit, B. Large-Scale Screening of Zeolite Structures for CO<sub>2</sub> Membrane Separations. *Journal of the American Chemical Society* **2013**, *135*, 7545–7552, PMID: 23654217.
- (19) Matito-Martos, I.; Martin-Calvo, A.; Gutiérrez-Sevillano, J. J.; Haranczyk, M.; Doblare, M.; Parra, J. B.; Ania, C. O.; Calero, S. Zeolite screening for the separation of gas mixtures containing SO<sub>2</sub>, CO<sub>2</sub> and CO. *Phys. Chem. Chem. Phys.* **2014**, *16*, 19884–19893.
- (20) Yilmaz, G.; Ozcan, A.; Keskin, S. Computational screening of ZIFs for CO<sub>2</sub> separations. *Molecular Simulation* **2015**, *41*, 713–726.
- (21) Tang, D.; Wu, Y.; Verploegh, R. J.; Sholl, D. S. Efficiently Exploring Adsorption Space to Identify Privileged Adsorbents for Chemical Separations of a Diverse Set of Molecules. *ChemSusChem* **2018**, *11*, 1567–1575.
- (22) Yan, T.; Lan, Y.; Tong, M.; Zhong, C. Screening and Design of Covalent Organic Framework Membranes for CO<sub>2</sub>/CH<sub>4</sub> Separation. *ACS Sustainable Chemistry & Engineering* **2019**, *7*, 1220–1227.
- (23) Lee, S.; Kim, B.; Cho, H.; Lee, H.; Lee, S. Y.; Cho, E. S.; Kim, J. Computational Screening of Trillions of Metal–Organic Frameworks for High-Performance Methane Storage. *ACS Applied Materials & Interfaces* **2021**, *13*, 23647–23654, PMID: 33988362.

- (24) Aydin, S.; Altintas, C.; Keskin, S. High-Throughput Screening of COF Membranes and COF/Polymer MMMs for Helium Separation and Hydrogen Purification. *ACS Applied Materials & Interfaces* **2022**, *14*, 21738–21749.
- (25) Schwalbe-Koda, D.; Kwon, S.; Paris, C.; Bello-Jurado, E.; Jensen, Z.; Olivetti, E.; Willhammar, T.; Corma, A.; Román-Leshkov, Y.; Moliner, M.; Gómez-Bombarelli, R. A priori control of zeolite phase competition and intergrowth with high-throughput simulations. *Science* **2021**, *374*, 308–315.
- (26) Chung, Y. G.; Camp, J.; Haranczyk, M.; Sikora, B. J.; Bury, W.; Krungleviciute, V.; Yildirim, T.; Farha, O. K.; Sholl, D. S.; Snurr, R. Q. Computation-Ready, Experimental Metal–Organic Frameworks: A Tool To Enable High-Throughput Screening of Nanoporous Crystals. *Chemistry of Materials* **2014**, *26*, 6185–6192.
- (27) Chung, Y. G.; Haldoupis, E.; Bucior, B. J.; Haranczyk, M.; Lee, S.; Zhang, H.; Vogiatzis, K. D.; Milisavljevic, M.; Ling, S.; Camp, J. S.; Slater, B.; Siepmann, J. I.; Sholl, D. S.; Snurr, R. Q. Advances, Updates, and Analytics for the Computation-Ready, Experimental Metal–Organic Framework Database: CoRE MOF 2019. *Journal of Chemical & Engineering Data* **2019**, *64*, 5985–5998.
- (28) Wilmer, C. E.; Leaf, M.; Lee, C. Y.; Farha, O. K.; Hauser, B. G.; Hupp, J. T.; Snurr, R. Q. Large-scale screening of hypothetical metal–organic frameworks. *Nature Chemistry* **2012**, *4*, 83–89.
- (29) Majumdar, S.; Moosavi, S. M.; Jablonka, K. M.; Ongari, D.; Smit, B. Diversifying Databases of Metal Organic Frameworks for High-Throughput Computational Screening. *ACS Applied Materials & Interfaces* **2021**, *13*, 61004–61014, PMID: 34910455.
- (30) Colón, Y. J.; Gómez-Gualdrón, D. A.; Snurr, R. Q. Topologically Guided, Automated Construction of Metal–Organic Frameworks and Their Evaluation for Energy-Related Applications. *Crystal Growth & Design* **2017**, *17*, 5801–5810.
- (31) Rosen, A. S.; Iyer, S. M.; Ray, D.; Yao, Z.; Aspuru-Guzik, A.; Gagliardi, L.; Notestein, J. M.; Snurr, R. Q. Machine learning the quantum-chemical properties of metal–organic frameworks for accelerated materials discovery. *Matter* **2021**, *4*, 1578–1597.
- (32) Pophale, R.; Cheeseman, P. A.; Deem, M. W. A database of new zeolite-like materials. *Phys. Chem. Chem. Phys.* **2011**, *13*, 12407–12412.
- (33) Dubbeldam, D.; Calero, S.; Ellis, D. E.; Snurr, R. Q. RASPA: molecular simulation software for adsorption and diffusion in flexible nanoporous materials. *Molecular Simulation* **2016**, *42*, 81–101.
- (34) Sharma, S.; Balestra, S. R. G.; Baur, R.; Agarwal, U.; Zuidema, E.; Rigutto, M. S.; Calero, S.; Vlugt, T. J. H.; Dubbeldam, D. RUPTURA: simulation code for breakthrough, ideal adsorption solution theory computations, and fitting of isotherm models. *Molecular Simulation* **2023**, *49*, 893–953.
- (35) Simon, C. M.; Smit, B.; Haranczyk, M. pyIAST: Ideal adsorbed solution theory (IAST) Python package. *Computer Physics Communications* **2016**, *200*, 364–380.
- (36) Thompson, A. P.; Aktulga, H. M.; Berger, R.; Bolintineanu, D. S.; Brown, W. M.; Crozier, P. S.; in 't Veld, P. J.; Kohlmeyer, A.; Moore, S. G.; Nguyen, T. D.; Shan, R.; Stevens, M. J.; Tranchida, J.; Trott, C.; Plimpton, S. J. LAMMPS - a flexible simulation tool for particle-based materials modeling at the atomic, meso, and continuum scales.



- (37) Shah, J. K.; Marin-Rimoldi, E.; Mullen, R. G.; Keene, B. P.; Khan, S.; Paluch, A. S.; Rai, N.; Romanielo, L. L.; Rosch, B.; Thomas W Yoo; Maginn, E. J. Cassandra: An open source Monte Carlo package for molecular simulation. *Journal of Computational Chemistry* **2017**, *38*, 1727–1739.
- (38) Simon, C. M.; Mercado, R.; Schnell, S. K.; Smit, B.; Haranczyk, M. What Are the Best Materials To Separate a Xenon/Krypton Mixture? *Chemistry of Materials* **2015**, *27*, 4459–4475.
- (39) Pardakhti, M.; Nanda, P.; Srivastava, R. Impact of Chemical Features on Methane Adsorption by Porous Materials at Varying Pressures. *The Journal of Physical Chemistry C* **2020**, *124*, 4534–4544.
- (40) Yu, X.; Choi, S.; Tang, D.; Medford, A. J.; Sholl, D. S. Efficient Models for Predicting Temperature-Dependent Henry’s Constants and Adsorption Selectivities for Diverse Collections of Molecules in Metal–Organic Frameworks. *The Journal of Physical Chemistry C* **2021**, *125*, 18046–18057.
- (41) Inverse design of nanoporous crystalline reticular materials with deep generative models. *Nature Machine Intelligence* **2021**, *3*, 76–86.
- (42) Bucior, B. J.; Bobbitt, N. S.; Islamoglu, T.; Goswami, S.; Gopalan, A.; Yildirim, T.; Farha, O. K.; Bagheri, N.; Snurr, R. Q. Energy-based descriptors to rapidly predict hydrogen storage in metal–organic frameworks. *Mol. Syst. Des. Eng.* **2019**, *4*, 162–174.
- (43) Yang, C.-T.; Pandey, I.; Trinh, D.; Chen, C.-C.; Howe, J. D.; Lin, L.-C. Deep learning neural network potential for simulating gaseous adsorption in metal–organic frameworks. *Mater. Adv.* **2022**, *3*, 5299–5303.
- (44) Dzubak, A. L.; Lin, L.-C.; Kim, J.; Swisher, J. A.; Poloni, R.; Maximoff, S. N.; Smit, B.; Gagliardi, L. Ab initio carbon capture in open-site metal–organic frameworks. *Nature Chemistry* **2012**, *4*, 801–816.
- (45) Cleeton, C.; de Oliveira, F. L.; Neumann, R.; Farmahini, A.; Luan, B.; Steiner, M.; Sarkisov, L. A process-level perspective of the impact of molecular force fields on the computational screening of MOFs for carbon capture. *ChemRxiv* **2023**,
- (46) Yazaydin, A. O.; Snurr, R. Q.; Park, T.-H.; Koh, K.; Liu, J.; LeVan, M. D.; Benin, A. I.; Jakubczak, P.; Lanuza, M.; Galloway, D. B.; Low, J. J.; Willis, R. R. Screening of Metal–Organic Frameworks for Carbon Dioxide Capture from Flue Gas Using a Combined Experimental and Modeling Approach. *Journal of the American Chemical Society* **2009**, *131*, 18198–18199.
- (47) Chen, L.; Morrison, C. A.; Düren, T. Improving Predictions of Gas Adsorption in Metal–Organic Frameworks with Coordinatively Unsaturated Metal Sites: Model Potentials, ab initio Parameterization, and GCMC Simulations. *J. Phys. Chem. C* **2012**, *116*, 18899–18909.
- (48) Becker, T. M.; Heinen, J.; Dubbel-dam, D.; Lin, L.-C.; Vlugt, T. J. H. Polarizable Force Fields for CO<sub>2</sub> and CH<sub>4</sub> Adsorption in M-MOF-74. *J. Phys. Chem. C* **2017**, *121*, 4659–4673.
- (49) Zhang, C.; Wang, L.; Maurin, G.; Yang, Q. In Silico Screening of MOFs with open copper sites for C<sub>2</sub>H<sub>2</sub>/CO<sub>2</sub> separation. *AIChE Journal* **2018**, *64*, 4089–4096.
- (50) Chung, Y. G.; Gómez-Gualdrón, D. A.; Li, P.; Leperi, K. T.; Deria, P.; Zhang, H.;

- Vermeulen, N. A.; Stoddart, J. F.; You, F.; Hupp, J. T.; Farha, O. K.; Snurr, R. Q. In silico discovery of metal-organic frameworks for precombustion CO<sub>2</sub> capture using a genetic algorithm. *Science Advances* **2016**, *2*, e1600909.
- (51) Deng, X.; Yang, W.; Li, S.; Liang, H.; Shi, Z.; Qiao, Z. Large-Scale Screening and Machine Learning to Predict the Computation-Ready, Experimental Metal-Organic Frameworks for CO<sub>2</sub> Capture from Air. *Applied Sciences* **2020**, *10*.
- (52) Bobbitt, N. S.; Shi, K.; Bucior, B. J.; Chen, H.; Tracy-Amoroso, N.; Li, Z.; Sun, Y.; Merlin, J. H.; Siepmann, J. I.; Siderius, D. W.; Snurr, R. Q. MOFX-DB: An Online Database of Computational Adsorption Data for Nanoporous Materials. *Journal of Chemical & Engineering Data* **2023**, *68*, 483–498.
- (53) Burner, J.; Luo, J.; White, A.; Mirmiran, A.; Kwon, O.; Boyd, P. G.; Maley, S.; Gibaldi, M.; Simrod, S.; Ogden, V.; Woo, T. K. ARC-MOF: A Diverse Database of Metal-Organic Frameworks with DFT-Derived Partial Atomic Charges and Descriptors for Machine Learning. *Chemistry of Materials* **2023**, *35*, 900–916.
- (54) Heindel, J. P.; Herman, K. M.; Xanthreas, S. S. Many-Body Effects in Aqueous Systems: Synergies Between Interaction Analysis Techniques and Force Field Development. *Annual Review of Physical Chemistry* **2023**, *74*, 337–360.
- (55) Steinmann, S. N.; Morais, R. F. D.; Götz, A. W.; Fleurat-Lessard, P.; Iannuzzi, M.; Sautet, P.; Michel, C. Force Field for Water over Pt(111): Development, Assessment, and Comparison. *Journal of Chemical Theory and Computation* **2018**, *14*, 3238–3251.
- (56) Brugnoli, L.; Menziani, M. C.; Urata, S.; Pedone, A. Development and Application of a ReaxFF Reactive Force Field for Cerium Oxide/Water Interfaces. *The Journal of Physical Chemistry A* **2021**, *125*, 5693–5708.
- (57) Lopes, P. E. M.; Murashov, V.; Tazi, M.; Demchuk, E.; MacKerell, A. D. Development of an Empirical Force Field for Silica. Application to the Quartz-Water Interface. *The Journal of Physical Chemistry B* **2006**, *110*, 2782–2792.
- (58) Nandy, A.; Terrones, G.; Arunachalam, N.; Duan, C.; Kastner, D. W.; Kulik, H. J. MOFSimplify, machine learning models with extracted stability data of three thousand metal-organic frameworks. *Scientific Data* **2022**, *9*, 74.
- (59) Park, H.; Majumdar, S.; Zhang, X.; Kim, J.; Smit, B. Inverse design of metal-organic frameworks for direct air capture of CO<sub>2</sub> via deep reinforcement learning. *ChemRxiv* **2023**,
- (60) Zhou, C.; Li, H.; Qin, H.; Yuan, B.; Zhang, M.; Wang, L.; Yang, B.; an Tao, C.; Zhang, S. Defective UiO-66-NH<sub>2</sub> monoliths for optimizing CO<sub>2</sub> capture performance. *Chemical Engineering Journal* **2023**, *467*, 143394.
- (61) Niu, J.; Li, H.; Tao, L.; Fan, Q.; Liu, W.; Tan, M. C. Defect Engineering of Low-Coordinated Metal-Organic Frameworks (MOFs) for Improved CO<sub>2</sub> Access and Capture. *ACS Applied Materials & Interfaces* **2023**, *15*, 31664–31674, PMID: 37350311.
- (62) Möslein, A. F.; Donà, L.; Civaleri, B.; Tan, J.-C. Defect Engineering in Metal-Organic Framework Nanocrystals: Implications for Mechanical Properties and Performance. *ACS Applied Nano Materials* **2022**, *5*, 6398–6409.
- (63) Gurnani, R.; Yu, Z.; Kim, C.; Sholl, D. S.; Ramprasad, R. Interpretable Machine Learning-Based Predictions of Methane Uptake Isotherms in

- Metal–Organic Frameworks. *Chemistry of Materials* **2021**, *33*, 3543–3552.
- (64) Anderson, R.; Biong, A.; Gómez-Gualdrón, D. A. Adsorption Isotherm Predictions for Multiple Molecules in MOFs Using the Same Deep Learning Model. *Journal of Chemical Theory and Computation* **2020**, *16*, 1271–1283, PMID: 31922755.
- (65) Choudhary, K.; Yildirim, T.; Siderius, D. W.; Kusne, A. G.; McDannald, A.; Ortiz-Montalvo, D. L. Graph neural network predictions of metal organic framework CO<sub>2</sub> adsorption properties. *Computational Materials Science* **2022**, *210*, 111388.
- (66) Fernandez, M.; Trefiak, N. R.; Woo, T. K. Atomic Property Weighted Radial Distribution Functions Descriptors of Metal–Organic Frameworks for the Prediction of Gas Uptake Capacity. *The Journal of Physical Chemistry C* **2013**, *117*, 14095–14105.
- (67) Li, Z.; Bucior, B. J.; Chen, H.; Haranczyk, M.; Siepmann, J. I.; Snurr, R. Q. Machine learning using host/guest energy histograms to predict adsorption in metal–organic frameworks: Application to short alkanes and Xe/Kr mixtures. *The Journal of Chemical Physics* **2021**, *155*, 014701.
- (68) Choi, S.; Sholl, D. S.; Medford, A. J. Gaussian approximation of dispersion potentials for efficient featurization and machine-learning predictions of metal–organic frameworks. *The Journal of Chemical Physics* **2022**, *156*, 214108.
- (69) Nandy, A.; Duan, C.; Kulik, H. J. Using Machine Learning and Data Mining to Leverage Community Knowledge for the Engineering of Stable Metal–Organic Frameworks. *Journal of the American Chemical Society* **2021**, *143*, 17535–17547, PMID: 34643374.
- (70) Moghadam, P. Z.; Rogge, S. M.; Li, A.; Chow, C.-M.; Wieme, J.; Moharrami, N.; Aragonés-Anglada, M.; Conduit, G.; Gomez-Gualdrón, D. A.; Van Speybroeck, V.; Fairen-Jimenez, D. Structure-Mechanical Stability Relations of Metal-Organic Frameworks via Machine Learning. *Matter* **2019**, *1*, 219–234.
- (71) Batra, R.; Chen, C.; Evans, T. G.; Walton, K. S.; Ramprasad, R. Prediction of water stability of metal–organic frameworks using machine learning. *Nature Machine Intelligence* **2020**, *2*, 704–710.
- (72) Luo, Y.; Bag, S.; Zaremba, O.; Cierpka, A.; Andreo, J.; Wuttke, S.; Friederich, P.; Tsotsalas, M. MOF synthesis prediction enabled by automatic data mining and machine learning. *Angewandte Chemie International Edition* **2022**, *61*.
- (73) Jensen, Z.; Kim, E.; Kwon, S.; Gani, T. Z. H.; Román-Leshkov, Y.; Moliner, M.; Corma, A.; Olivetti, E. A Machine Learning Approach to Zeolite Synthesis Enabled by Automatic Literature Data Extraction. *ACS Cent. Sci.* **2019**, *5*, 892–899.
- (74) Moliner, M.; Román-Leshkov, Y.; Corma, A. Machine Learning Applied to Zeolite Synthesis: The Missing Link for Realizing High-Throughput Discovery. *Acc. Chem. Res.* **2019**, *52*, 2971–2980.
- (75) Chanussot\*, L.; Das\*, A.; Goyal\*, S.; Lavril\*, T.; Shuaibi\*, M.; Riviere, M.; Tran, K.; Heras-Domingo, J.; Ho, C.; Hu, W., et al. Open Catalyst 2020 (OC20) dataset and community challenges. *ACS Catalysis* **2021**, *11*, 6059–6072.
- (76) Nandy, A.; Yue, S.; Oh, C.; Duan, C.; Terrones, G. G.; Chung, Y. G.; Kulik, H. J. A database of ultrastable MOFs reassembled from stable fragments with

- machine learning models. *Matter* **2023**, *6*, 1585–1603.
- (77) Groom, C. R.; Bruno, I. J.; Lightfoot, M. P.; Ward, S. C. The Cambridge Structural Database. *Acta Crystallographica Section B* **2016**, *72*, 171–179.
- (78) Nazarian, D.; Ganesh, P.; Sholl, D. S. Benchmarking density functional theory predictions of framework structures and properties in a chemically diverse test set of metal–organic frameworks. *Journal of Materials Chemistry A* **2015**, *3*, 22432–22440.
- (79) Chen, T.; Manz, T. A. Identifying misbonded atoms in the 2019 CoRE metal–organic framework database. *RSC Advances* **2020**, *10*, 26944–26951.
- (80) Moosavi, S. M.; Nandy, A.; Jablonka, K. M.; Ongari, D.; Janet, J. P.; Boyd, P. G.; Lee, Y.; Smit, B.; Kulik, H. J. Understanding the diversity of the metal-organic framework ecosystem. *Nature Communications* **2020**, *11*, 4068.
- (81) Perdew, J. P.; Burke, K.; Ernzerhof, M. Generalized gradient approximation made simple. *Physical Review Letters* **1996**, *77*, 3865.
- (82) Grimme, S.; Antony, J.; Ehrlich, S.; Krieg, H. A consistent and accurate ab initio parametrization of density functional dispersion correction (DFT-D) for the 94 elements H-Pu. *Journal of Chemical Physics* **2010**, *132*, 154104.
- (83) Grimme, S.; Ehrlich, S.; Goerigk, L. Effect of the Damping Function in Dispersion Corrected Density Functional Theory. *Journal of Computational Chemistry* **2011**, *32*, 1456–1465.
- (84) Rosen, A. S.; Notestein, J. M.; Snurr, R. Q. Comparing GGA, GGA+U, and meta-GGA functionals for redox-dependent binding at open metal sites in metal–organic frameworks. *Journal of Chemical Physics* **2020**, *152*, 224101.
- (85) Yu, Z.; Jamdade, S.; Yu, X.; Cai, X.; Sholl, D. S. Efficient Generation of Large Collections of Metal-Organic Framework Structures Containing Well-Defined Point Defects. *The Journal of Physical Chemistry Letters* **2023**, *14*, 6658–6665.
- (86) Tran\*, R. et al. The Open Catalyst 2022 (OC22) Dataset and Challenges for Oxide Electrocatalysts. *ACS Catalysis* **2023**, *13*, 3066–3084.
- (87) Li, S.; Chung, Y. G.; Snurr, R. Q. High-throughput screening of metal–organic frameworks for CO<sub>2</sub> capture in the presence of water. *Langmuir* **2016**, *32*, 10368–10376.
- (88) Li, W.; Rao, Z.; Chung, Y. G.; Li, S. The role of partial atomic charge assignment methods on the computational screening of metal-organic frameworks for CO<sub>2</sub> capture under humid conditions. *ChemistrySelect* **2017**, *2*, 9458–9465.
- (89) Kancharlapalli, S.; Snurr, R. Q. High-throughput screening of the core-MOF-2019 database for CO<sub>2</sub> capture from wet flue gas: A multi-scale modeling strategy. *ACS Applied Materials Interfaces* **2023**, *15*, 28084–28092.
- (90) Hernandez, A. F.; Impastato, R. K.; Hossain, M. I.; Rabideau, B. D.; Glover, T. G. Water bridges substitute for defects in amine-functionalized uio-66, boosting CO<sub>2</sub> adsorption. *Langmuir* **2021**, *37*, 10439–10449.
- (91) Hossain, M. I.; Cunningham, J. D.; Becker, T. M.; Grabicka, B. E.; Walton, K. S.; Rabideau, B. D.; Glover, T. G. Impact of MOF defects on the binary adsorption of CO<sub>2</sub> and water in Uio-66. *Chemical Engineering Science* **2019**, *203*, 346–357.
- (92) Yazaydin, A. O.; Benin, A. I.; Faheem, S. A.; Jakubczak, P.; Low, J. J.;

- Willis, R. R.; Snurr, R. Q. Enhanced CO<sub>2</sub> adsorption in metal-organic frameworks via occupation of open-metal sites by coordinated water molecules. *Chemistry of Materials* **2009**, *21*, 1425–1430.
- (93) Liao, P.-Q.; Zhou, D.-D.; Zhu, A.-X.; Jiang, L.; Lin, R.-B.; Zhang, J.-P.; Chen, X.-M. Strong and dynamic CO<sub>2</sub> sorption in a flexible porous framework possessing guest chelating claws. *Journal of the American Chemical Society* **2012**, *134*, 17380–17383.
- (94) Li, T.; Yang, J.; Hong, X.-J.; Ou, Y.-J.; Gu, Z.-G.; Cai, Y.-P. A robust porous pillar-chained CD-framework with Selective Sorption for CO<sub>2</sub> and guest-driven tunable luminescence. *CrystEngComm* **2014**, *16*, 3848.
- (95) Zhang, M.; Chen, Y.-P.; Zhou, H.-C. Structural design of porous coordination networks from Tetrahedral Building Units. *CrystEngComm* **2013**,
- (96) Hua, J.; Wang, M.; Zhang, D.; Pei, X.; Zhao, X.; Ma, X. A three-dimensional cadmium mixed ligands coordination polymer with CO<sub>2</sub> adsorption ability. *Journal of Structural Chemistry* **2022**, *63*, 2045–2053.
- (97) Xue, Z.; Sheng, T.; Wang, Y.; Hu, S.; Wen, Y.; Wang, Y.; Li, H.; Fu, R.; Wu, X. A series of d<sup>10</sup> coordination polymers constructed with a rigid tripodal imidazole ligand and varied polycarboxylates: Syntheses, structures and luminescence properties. *CrystEngComm* **2015**, *17*, 2004–2012.
- (98) Navarro, J. A.; Barea, E.; Salas, J. M.; Masciocchi, N.; Galli, S.; Sironi, A.; Ania, C. O.; Parra, J. B. H<sub>2</sub>, N<sub>2</sub>, CO, and CO<sub>2</sub> sorption properties of a series of robust sodalite-type microporous coordination polymers. *Inorganic Chemistry* **2006**, *45*, 2397–2399.
- (99) Tabares, L. C.; Navarro, J. A.; Salas, J. M. Cooperative guest inclusion by a zeolite analogue coordination polymer. sorption behavior with gases and amine and Group 1 Metal salts. *Journal of the American Chemical Society* **2000**, *123*, 383–387.
- (100) Xue, Y.-S.; He, Y.; Ren, S.-B.; Yue, Y.; Zhou, L.; Li, Y.-Z.; Du, H.-B.; You, X.-Z.; Chen, B. A robust microporous metal-organic framework constructed from a flexible organic linker for acetylene storage at ambient temperature. *Journal of Materials Chemistry* **2012**, *22*, 10195.
- (101) Chen, J.; Wang, S.-H.; Liu, Z.-F.; Wu, M.-F.; Xiao, Y.; Zheng, F.-K.; Guo, G.-C.; Huang, J.-S. Anion-directed self-assembly of Cu(II) coordination compounds with tetrazole-1-acetic acid: Syntheses in ionic liquids and crystal structures. *New J. Chem.* **2014**, *38*, 269–276.
- (102) Ding, D.-G.; Xu, H.; Fan, Y.-T.; Hou, H.-W. Anion-dependent assemblies of two unprecedented copper(ii) polymers with four-fold screw axes and trapped sodium chains. *Inorganic Chemistry Communications* **2008**, *11*, 1280–1283.
- (103) Liu, D.; Li, M.; Li, D. Reversible solid-gas chemical equilibrium between a 0-periodic deformable molecular tecton and a 3-periodic coordination architecture. *Chemical Communications* **2009**, 6943.
- (104) Vaidhyanathan, R.; Bradshaw, D.; Rebilly, J.-N.; Barrio, J. P.; Gould, J. A.; Berry, N. G.; Rosseinsky, M. J. A family of nanoporous materials based on an amino acid backbone. *Angewandte Chemie International Edition* **2006**, *45*, 6495–6499.
- (105) Kanoo, P.; Gurunatha, K. L.; Maji, T. K. Versatile functionalities in mofs assembled from the same building units: Interplay of structural flexibility, rigidity

- and regularity. *J. Mater. Chem.* **2010**, *20*, 1322–1331.
- (106) Zhao, D.; Yuan, D.; Yakovenko, A.; Zhou, H.-C. A NBO-type metal–organic framework derived from a polyyne-coupled di-isophthalate linker formed in situ. *Chemical Communications* **2010**, *46*, 4196.
- (107) Shao, K.; Pei, J.; Wang, J.-X.; Yang, Y.; Cui, Y.; Zhou, W.; Yildirim, T.; Li, B.; Chen, B.; Qian, G. Tailoring the pore geometry and chemistry in microporous metal–organic frameworks for high methane storage working capacity. *Chemical Communications* **2019**, *55*, 11402–11405.
- (108) Mahajan, S.; Lahtinen, M. Recent progress in metal-organic frameworks (MOFs) for CO<sub>2</sub> capture at different pressures. *Journal of Environmental Chemical Engineering* **2022**, *10*, 108930.
- (109) Rappe, A. K.; Casewit, C. J.; Colwell, K. S.; Goddard, W. A.; Skiff, W. M. UFF, a full periodic table force field for molecular mechanics and molecular dynamics simulations. *Journal of the American Chemical Society* **1992**, *114*, 10024–10035.
- (110) Addicoat, M. A.; Vankova, N.; Akter, I. F.; Heine, T. Extension of the Universal Force Field to Metal-Organic Frameworks. *Journal of Chemical Theory and Computation* **2014**, *10*, 880–891.
- (111) Coupry, D. E.; Addicoat, M. A.; Heine, T. Extension of the Universal Force Field for Metal-Organic Frameworks. *Journal of Chemical Theory and Computation* **2016**, *12*, 5215–5225.
- (112) Eggimann, B. L.; Sunnarborg, A. J.; Stern, H. D.; Bliss, A. P.; Siepmann, J. I. An online parameter and property database for the TraPPE force field. *Molecular Simulation* **2014**, *40*, 101–105.
- (113) Berendsen, H. J. C.; Grigera, J. R.; Straatsma, T. P. The missing term in effective pair potentials. *The Journal of Physical Chemistry* **1987**, *91*, 6269–6271.
- (114) Manz, T. A.; Sholl, D. S. Chemically Meaningful Atomic Charges That Reproduce the Electrostatic Potential in Periodic and Nonperiodic Materials. *Journal of Chemical Theory and Computation* **2010**, *6*, 2455–2468, PMID: 26613499.
- (115) Yu, Z.; Anstine, D. M.; Boulfelfel, S. E.; Gu, C.; Colina, C. M.; Sholl, D. S. Incorporating Flexibility Effects into Metal–Organic Framework Adsorption Simulations Using Different Models. *ACS Applied Materials & Interfaces* **2021**, *13*, 61305–61315, PMID: 34927436.
- (116) Colón, Y. J.; Fairen-Jimenez, D.; Wilmer, C. E.; Snurr, R. Q. High-Throughput Screening of Porous Crystalline Materials for Hydrogen Storage Capacity near Room Temperature. *The Journal of Physical Chemistry C* **2014**, *118*, 5383–5389.
- (117) Zielkiewicz, J. Structural properties of water: Comparison of the SPC, SPCE, TIP4P, and TIP5P models of water. *The Journal of Chemical Physics* **2005**, *123*, 104501.
- (118) Schütt, K.; Kindermans, P.-J.; Felix, H. E. S.; Chmiela, S.; Tkatchenko, A.; Müller, K.-R. Schnet: A continuous-filter convolutional neural network for modeling quantum interactions. *Advances in Neural Information Processing Systems*. 2017; pp 991–1001.
- (119) Gasteiger, J.; Groß, J.; Günnemann, S. Directional Message Passing for Molecular Graphs. *International Conference on Learning Representations*. 2020.
- (120) Schütt, K.; Unke, O.; Gastegger, M. Equivariant message passing for the prediction of tensorial properties and molec-

- ular spectra. International Conference on Machine Learning. 2021; pp 9377–9388.
- (121) Gasteiger, J.; Shuaibi, M.; Sriram, A.; Günnemann, S.; Ulissi, Z.; Zitnick, C. L.; Das, A. GemNet-OC: Developing Graph Neural Networks for Large and Diverse Molecular Simulation Datasets. *Transactions on Machine Learning Research (TMLR)* **2022**,
- (122) Passaro, S.; Zitnick, C. L. Reducing SO(3) Convolutions to SO(2) for Efficient Equivariant GNNs. 2023.
- (123) Liao, Y.-L.; Wood, B.; Das\*, A.; Smidt\*, T. EquiformerV2: Improved Equivariant Transformer for Scaling to Higher-Degree Representations. 2023.
- (124) Kulkarni, A. R.; Sholl, D. S. Screening of Copper Open Metal Site MOFs for Olefin/Paraffin Separations Using DFT-Derived Force Fields. *The Journal of Physical Chemistry C* **2016**, *120*, 23044–23054.
- (125) Hestness, J.; Narang, S.; Ardalani, N.; Diamos, G.; Jun, H.; Kianinejad, H.; Patwary, M. M. A.; Yang, Y.; Zhou, Y. Deep Learning Scaling is Predictable, Empirically. 2017.
- (126) Kaplan, J.; McCandlish, S.; Henighan, T.; Brown, T. B.; Chess, B.; Child, R.; Gray, S.; Radford, A.; Wu, J.; Amodei, D. Scaling Laws for Neural Language Models. 2020.
- (127) Hoffmann, J. et al. Training Compute-Optimal Large Language Models. 2022.
- (128) Batzner, S.; Musaelian, A.; Sun, L.; Geiger, M.; Mailoa, J. P.; Kornbluth, M.; Molinari, N.; Smidt, T. E.; Kozinsky, B. E (3)-equivariant graph neural networks for data-efficient and accurate interatomic potentials. *Nature Communications* **2022**, *13*, 1–11.
- (129) Tran, K.; Neiswanger, W.; Yoon, J.; Zhang, Q.; Xing, E.; Ulissi, Z. W. Methods for comparing uncertainty quantifications for material property predictions. *Machine Learning: Science and Technology* **2020**, *1*, 025006.
- (130) Shuaibi, M.; Sivakumar, S.; Chen, R. Q.; Ulissi, Z. W. Enabling robust offline active learning for machine learning potentials using simple physics-based priors. *Machine Learning: Science and Technology* **2020**, *2*, 025007.
- (131) Ramakrishnan, R.; Dral, P. O.; Rupp, M.; von Lilienfeld, O. A. Big data meets quantum chemistry approximations: the  $\Delta$ -machine learning approach. *Journal of Chemical Theory and Computation* **2015**, *11*, 2087–2096.
- (132) Crawshaw, M. Multi-Task Learning with Deep Neural Networks: A Survey. 2020.
- (133) Tan, C.; Sun, F.; Kong, T.; Zhang, W.; Yang, C.; Liu, C. A Survey on Deep Transfer Learning. 2018.
- (134) Kresse, G.; Furthmüller, J. Efficiency of ab-initio total energy calculations for metals and semiconductors using a plane-wave basis set. *Computational Materials Science* **1996**, *6*, 15–50.
- (135) Bucior, B. J.; Rosen, A. S.; Haranczyk, M.; Yao, Z.; Ziebel, M. E.; Farha, O. K.; Hupp, J. T.; Siepmann, J. I.; Aspuru-Guzik, A.; Snurr, R. Q. Identification Schemes for Metal–Organic Frameworks To Enable Rapid Search and Cheminformatics Analysis. *Crystal Growth & Design* **2019**, *19*, 6682–6697.
- (136) Potoff, J. J.; Siepmann, J. I. Vapor–liquid equilibria of mixtures containing alkanes, carbon dioxide, and nitrogen. *AIChE Journal* **2001**, *47*, 1676–1682.
- (137) Mahoney, M. W.; Jorgensen, W. L. A five-site model for liquid water and the

reproduction of the density anomaly by rigid, nonpolarizable potential functions. *The Journal of Chemical Physics* **2000**, *112*, 8910–8922.

- (138) Rick, S. W. A reoptimization of the five-site water potential (TIP5P) for use with Ewald sums. *The Journal of Chemical Physics* **2004**, *120*, 6085–6093.
- (139) Boyd, P. G.; Moosavi, S. M.; Witman, M.; Smit, B. Force-Field Prediction of Materials Properties in Metal-Organic Frameworks. *The Journal of Physical Chemistry Letters* **2017**, *8*, 357–363.
- (140) Shuaibi, M.; Kolluru, A.; Das, A.; Grover, A.; Sriram, A.; Ulissi, Z.; Zitnick, C. L. Rotation invariant graph neural networks using spin convolutions. *arXiv preprint* **2021**, *arXiv:2106.09575 [cs.LG]*.
- (141) Sriram, A.; Das, A.; Wood, B. M.; Goyal, S.; Zitnick, C. L. Towards training billion parameter graph neural networks for atomic simulations. International Conference on Learning Representations. 2022 (Accepted).
- (142) Gasteiger, J.; Becker, F.; Günnemann, S. GemNet: Universal directional graph neural networks for molecules. *Advances in Neural Information Processing Systems*. 2021; pp 6790–6802.
- (143) Paszke, A.; Gross, S.; Massa, F.; Lerer, A.; Bradbury, J.; Chanan, G.; Killeen, T.; Lin, Z.; Gimelshein, N.; Antiga, L., et al. Pytorch: An imperative style, high-performance deep learning library. *Advances in Neural Information Processing Systems*. 2019; pp 8026–8037.
- (144) Gasteiger, J.; Giri, S.; Margraf, J. T.; Günnemann, S. Fast and Uncertainty-Aware Directional Message Passing for Non-Equilibrium Molecules. *arXiv preprint* **2020**, *arXiv:2011.14115[cs.LG]*.



# Supplementary Information

## The Open DAC 2023 Dataset and Challenges for Sorbent Discovery in Direct Air Capture

### Supplementary Figures

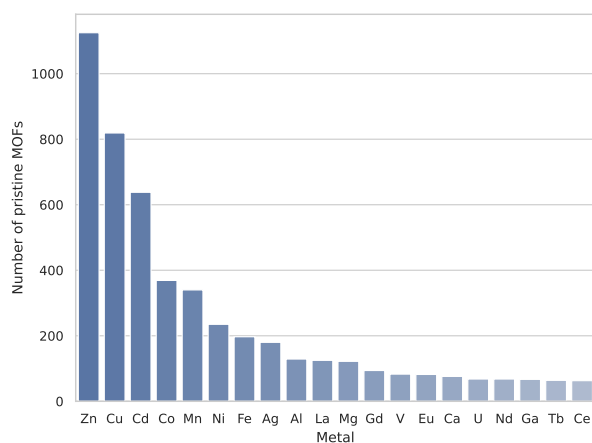


Figure S1: Top 20 metal atoms in pristine MOFs.

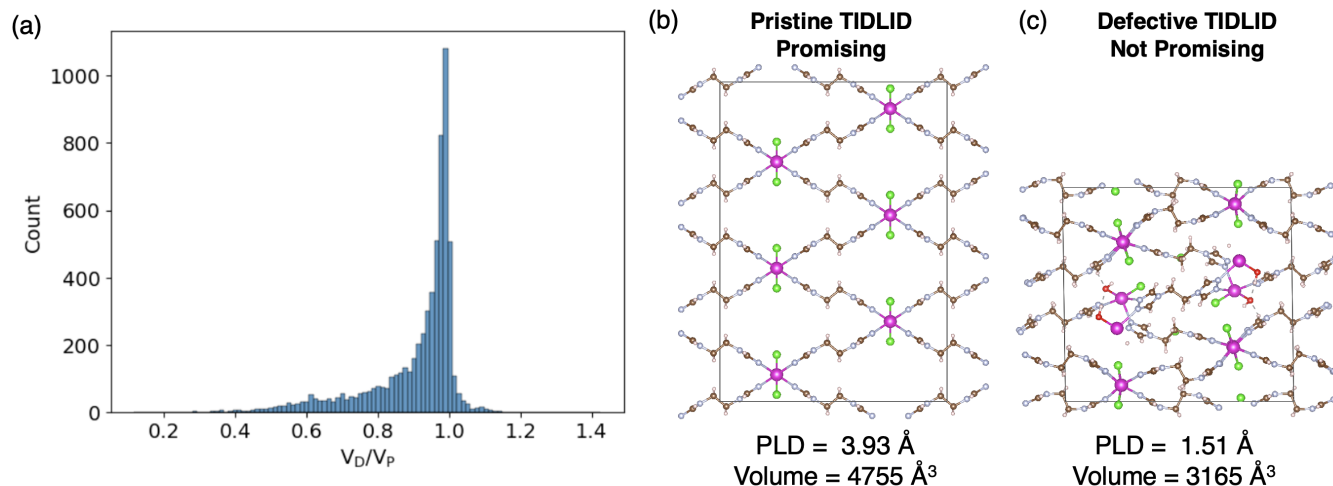


Figure S2: (a) A histogram of the ratio of the defective MOF volume ( $V_D$ ) over the pristine MOF volume ( $V_P$ ), with all structures fully DFT relaxed. The structure of relaxed (b) pristine and (c) defective TIDLID with a defect concentration of 0.08, showing structural collapse on defect formation.

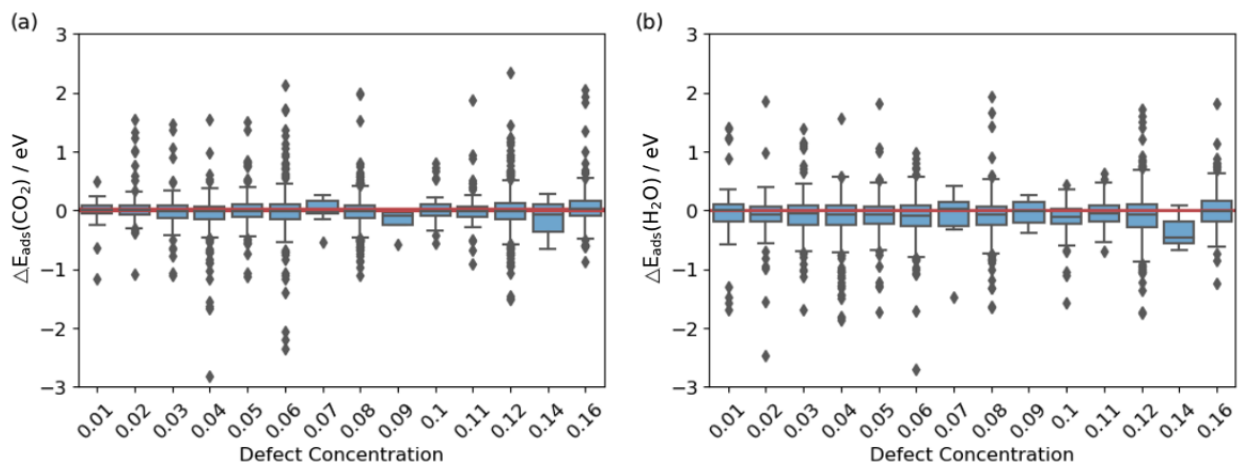


Figure S3: The influence of defect concentration on the adsorption energies of (a)  $\text{CO}_2$  and (b)  $\text{H}_2\text{O}$  in MOFs.  $\Delta E = E_{\text{Defective}} - E_{\text{Pristine}}$ .

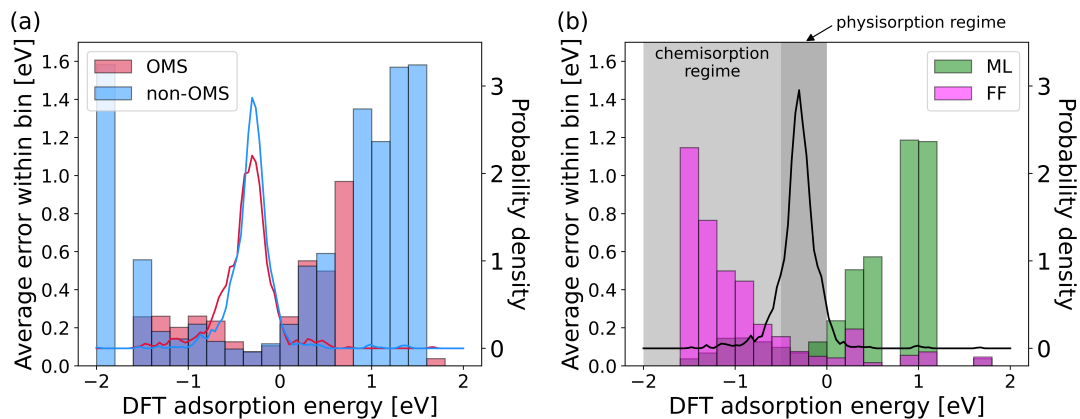


Figure S4: Binned errors and relative density of the number of points (solid lines) as a function of DFT adsorption energy for (a) ML predicted adsorption energies on open metal site (OMS) (red) and non-OMS (blue) and (b) interaction energies predicted by FFs (magenta) and corresponding adsorption energies predicted by ML (green) models. This plot is an extension of Fig. 7, displaying DFT adsorption energies within the range of -2 eV to 2 eV.

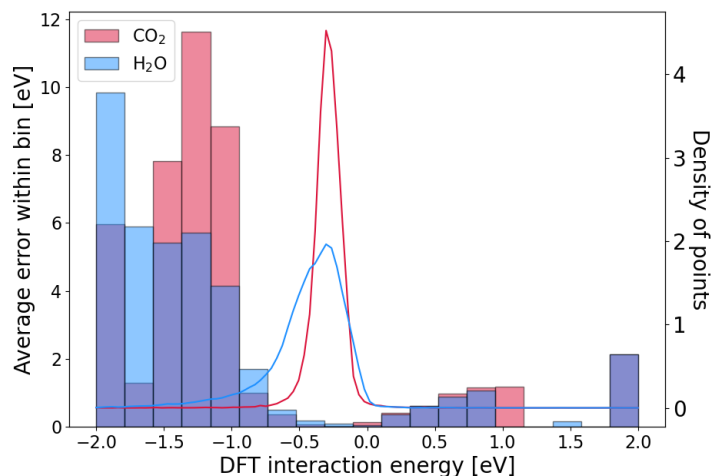


Figure S5: Binned FF errors and DFT interaction energy distributions split by adsorbate for all 51,252 systems with  $-2 \leq E_{\text{int}}^{\text{DFT}} \leq 2$  eV irrespective of FF interaction energy.

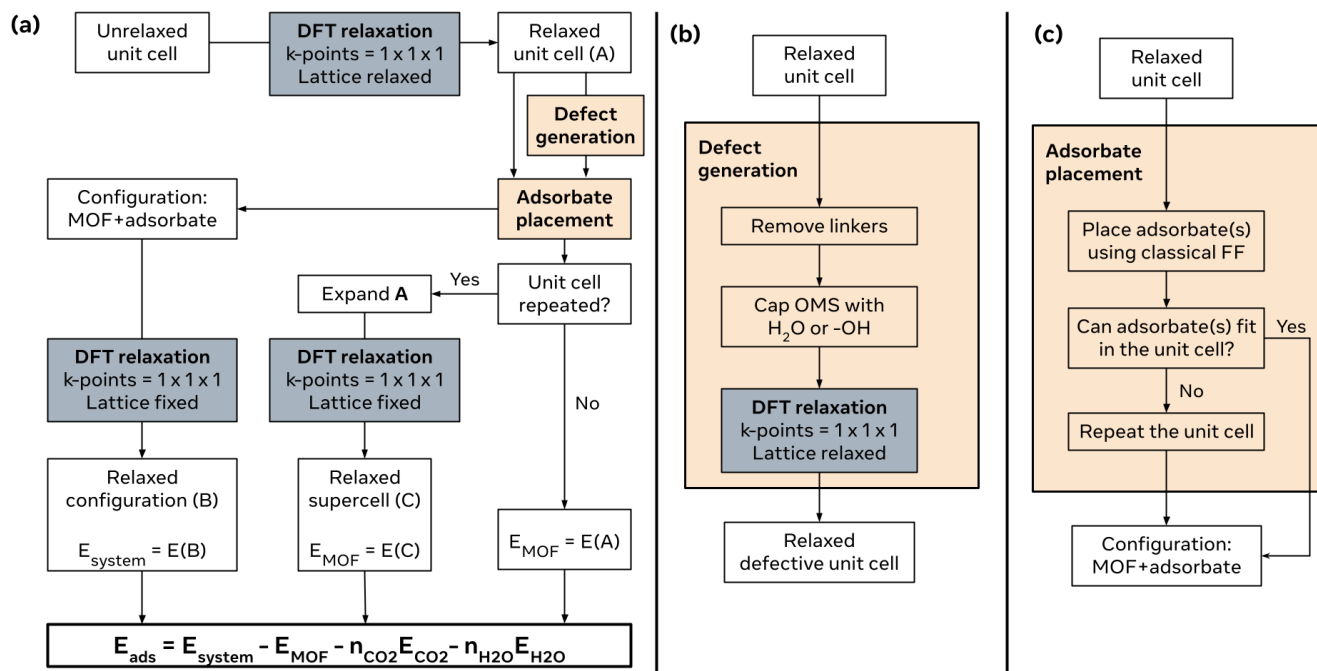


Figure S6: The workflow for generating and relaxing pristine and defective MOF structures in ODAC23.

# Supplementary Tables

Table S1: Summary of ODAC23 dataset organised by task and split

Task	Split	MOF + CO <sub>2</sub>	MOF + H <sub>2</sub> O	MOF + CO <sub>2</sub> + H <sub>2</sub> O	MOF + CO <sub>2</sub> + 2H <sub>2</sub> O	Total
S2EF	train	6,608,649	5,196,597	13,092,633	10,973,416	35,871,295
	val	160,841	125,984	310,093	242,647	839,565
	test-id	163,574	133,372	360,413	316,156	973,515
	test-ood (big)	62,718	63,711	136,374	118,416	381,219
	test-ood (linker)	50,392	14,242	99,376	123,115	287,125
	test-ood (topology)	71,384	60,308	182,255	158,309	472,256
	test-ood (linker & topology)	27,281	24,351	60,121	47,020	158,773
	<b>Total</b>		<b>7,144,839</b>	<b>5,618,565</b>	<b>14,241,265</b>	<b>11,979,079</b>
IS2RE/IS2RS	train	46,274	34,456	48,373	33,121	162,224
	val	1,138	862	1,211	787	3,998
	test-id	1,291	972	1,420	986	4,669
	test-ood (big)	533	383	534	318	1,768
	test-ood (linker)	355	87	383	357	1,182
	test-ood (topology)	439	306	533	334	1,612
	test-ood (linker & topology)	166	135	172	106	579
	<b>Total</b>		<b>50,196</b>	<b>37,201</b>	<b>52,626</b>	<b>36,009</b>

Table S2: Top 7 organic linkers in the pristine MOFs

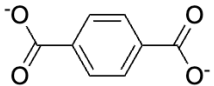
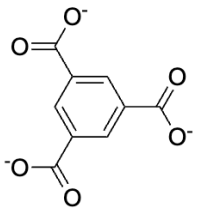

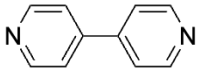
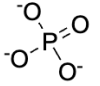
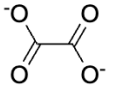
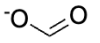
SMILES	Structure	Number of Pristine MOFs
<chem>[O-]C(=O)c1ccc(cc1)C(=O)[O-]</chem>		316
<chem>[O-]C(=O)c1cc(cc(c1)C(=O)[O-])C(=O)[O-]</chem>		244
<chem>C#N</chem>		220
<chem>n1ccc(cc1)c1ccncc1</chem>		216
<chem>[O-]P(=O)([O-])[O-]</chem>		157
<chem>[O-]C(=O)C(=O)[O-]</chem>		151
<chem>[O-]C=O</chem>		99

Table S3: Top 10 promising pristine MOFs with stronger CO<sub>2</sub> adsorption energy compared to H<sub>2</sub>O by DFT calculations [eV]

MOF	$E_{\text{ads}}(\text{CO}_2)$	$E_{\text{ads}}(\text{H}_2\text{O})$	$E_{\text{ads}}(\text{CO}_2) - E_{\text{ads}}(\text{H}_2\text{O})\uparrow$	$E_{\text{ads}}(\text{CO}_2 + \text{H}_2\text{O})$	$E_{\text{inter.mol}}^{\text{1st}}$	$E_{\text{ads}}(\text{CO}_2 + 2\text{H}_2\text{O})$	$E_{\text{inter.mol}}^{\text{2nd}}$
IPIDUH	-1.98	0.32	-2.30	-0.63	1.04	-2.51	-2.20
KOQLUZ	-1.50	0.70	-2.19	-3.11	-2.31	-3.54	-1.13
LEWZET	-0.89	0.81	-1.69	0.14	0.23	-4.53	-5.48
TUGTAR	-1.74	-0.47	-1.27	-1.70	0.51		
cm503311x.alf175K	-0.64	0.48	-1.12	-0.03	0.13	-2.20	-2.66
TONWUO	-1.71	-0.63	-1.09	-2.68	-0.34	-3.78	-0.48
IMAGAG	-1.14	-0.07	-1.07	-1.85	-0.64		
EGIFUV	-1.45	-0.41	-1.04	-0.43	1.42	-0.87	-0.03
ZIDBEV	-1.91	-0.91	-1.00	-2.83	0.00	-4.40	-0.66
PETWIW	-0.72	0.28	-0.99	-1.38	-0.93	-1.09	0.01

Table S4: Top 10 promising defective MOFs with stronger CO<sub>2</sub> adsorption energy compared to H<sub>2</sub>O by DFT calculations [eV]

MOF	Defect conc.	$E_{\text{ads}}(\text{CO}_2)$	$E_{\text{ads}}(\text{H}_2\text{O})$	$E_{\text{ads}}(\text{CO}_2) - E_{\text{ads}}(\text{H}_2\text{O})\uparrow$	$E_{\text{ads}}(\text{CO}_2 + \text{H}_2\text{O})$	$E_{\text{inter.mol}}^{\text{1st}}$	$E_{\text{ads}}(\text{CO}_2 + 2\text{H}_2\text{O})$	$E_{\text{inter.mol}}^{\text{2nd}}$
AFENEE	0.12	-1.86	-0.34	-1.52	-0.81	1.40	-1.65	-0.50
OKIXIQ_charged	0.12	-1.29	-0.09	-1.20	-1.09	0.29	-0.86	0.31
IDAGEA_charged	0.06	-1.18	-0.25	-0.93	-1.23	0.21	-2.42	-0.94
PEGCAH	0.06	-1.60	-0.77	-0.83	-2.83	-0.47	-3.13	0.46
COTXEQ	0.12	-0.60	0.15	-0.74	-1.05	-0.59	-1.56	-0.66
ODAHIK_charged	0.12	-1.02	-0.30	-0.71	-1.60	-0.28	-1.97	-0.06
HUWDEJ	0.12	-1.36	-0.65	-0.71	-1.19	0.82	-2.30	-0.46
HAJLUA	0.16	-0.93	-0.26	-0.68	-3.83	-2.64	-1.95	2.14
HAJLOU	0.16	-1.02	-0.35	-0.67	-1.80	-0.43	-4.32	-2.16
MALRUM	0.04	-1.29	-0.65	-0.64	-2.14	-0.20	-2.86	-0.07

Table S5: List of ML model architectures used in this work and the different tasks they were used for

List of ODAC23 Models							
Model	# of Parameters	Equivariant Reps	Tasks				
			S2EF	IS2RE-direct	IS2RE-Relax	IS2RS	
SchNet <sup>118</sup>	9.1M	✗	✓	*	*	*	
DimeNet++ <sup>144</sup>	1.8M	✗	✓	*	*	*	
PaiNN <sup>120</sup>	20.1M	✓	✓	*	*	*	
GemNet-OC <sup>121</sup>	38.9M	✗	✓	✓	✓	✓	
eSCN <sup>122</sup>	51.6M	✓	✓	✓	✓	✓	
EquiformerV2 <sup>123</sup>	31.1M	✓	✓	✓	✓	✓	
EquiformerV2 (large) <sup>123</sup>	153M	✓	✓	✓	✓	✓	

\* Skipped because S2EF results were not competitive

Table S6: Results on the S2EF task for the various test splits

Structure to Energy and Forces ( <i>S2EF</i> ) Test					
Split	Model	Force MAE [meV/Å] ↓	Force Cos ↑	Energy MAE [eV] ↓	EFwT ↑
test-id	Median baseline	16.02	0.001	0.406	0.00%
	SchNet	14.44	0.254	0.368	0.02%
	DimeNet++	14.31	0.226	0.416	0.02%
	PaiNN	13.04	0.345	0.241	0.11%
	GemNet-OC	9.87	0.605	0.153	1.16%
	eSCN	9.15	0.658	0.165	1.84%
	EquiformerV2	7.26	0.674	0.182	1.97%
	EquiformerV2 (large)	8.20	0.685	0.145	2.61%
test-ood(b)	Median baseline	7.98	0.001	0.334	0.00%
	SchNet	8.16	0.146	0.529	0.00%
	DimeNet++	7.85	0.157	0.728	0.00%
	PaiNN	7.53	0.242	0.282	0.12%
	GemNet-OC	6.19	0.495	0.207	0.81%
	eSCN	5.62	0.559	0.170	1.15%
	EquiformerV2	4.91	0.610	0.166	1.92%
	EquiformerV2 (large)	4.75	0.612	0.135	3.07%
test-ood(l)	Median baseline	14.65	0.000	0.378	0.00%
	Schnet	13.36	0.262	0.474	0.00%
	Dimenet++	12.15	0.253	0.501	0.01%
	PaiNN	11.47	0.378	0.252	0.05%
	Gemnet-OC	8.98	0.640	0.182	0.29%
	eSCN	7.69	0.719	0.179	0.59%
	EquiformerV2	6.85	0.760	0.161	1.36%
	EquiformerV2 (Large)	6.42	0.761	0.175	2.03%
test-ood(t)	Median baseline	16.18	0.000	0.677	0.00%
	SchNet	14.83	0.181	1.001	0.00%
	DimeNet++	13.62	0.183	1.297	0.00%
	PaiNN	18.18	0.267	0.507	0.01%
	GemNet-OC	12.59	0.488	0.312	0.05%
	eSCN	12.79	0.560	0.370	0.09%
	EquiformerV2	10.19	0.617	0.341	0.52%
	EquiformerV2 (large)	8.80	0.631	0.292	0.51%
test-ood(lt)	Median baseline	13.71	0.000	0.528	0.00%
	SchNet	13.23	0.234	0.746	0.00%
	DimeNet++	12.44	0.234	0.886	0.00%
	PaiNN	11.97	0.349	0.417	0.00%
	GemNet-OC	10.22	0.589	0.335	0.05%
	eSCN	8.78	0.680	0.305	0.25%
	EquiformerV2	7.31	0.727	0.302	0.52%
	EquiformerV2 (large)	7.20	0.720	0.316	0.48%

Table S7: Comparison of S2EF metrics for MOFs with and without OMSs.

<i>S2EF</i> Test - Open Metal Sites				
Model	OMS		Non-OMS	
	Energy MAE [eV] ↓	Force MAE [meV/Å] ↓	Energy MAE [eV] ↓	Force MAE [meV/Å] ↓
Median baseline	0.433	16.25	0.355	15.50
GemNet-OC	0.164	10.04	0.129	9.47
eSCN	0.186	9.29	0.120	8.82
EquiformerV2	0.204	8.18	0.169	6.85

Table S8: Comparison of S2EF metrics for pristine and defective MOFs.

<i>S2EF</i> Test - Pristine vs Defective				
Model	Pristine		Defective	
	Energy MAE [eV] ↓	Force MAE [meV/Å] ↓	Energy MAE [eV] ↓	Force MAE [meV/Å] ↓
Median baseline	0.406	16.02	0.395	12.12
GemNet-OC	0.153	9.87	0.182	8.05
eSCN	0.165	9.15	0.199	7.36
EquiformerV2	0.187	8.11	0.176	6.58

Table S9: Full results of metrics for IS2RE task on all data splits.

Initial Structure to Relaxed Energy ( <i>IS2RE</i> ) Test				
Split	Method	Model	Energy MAE [eV] ↓	EwT ↑
test-id	Direct	GemNet-OC	0.181	10.40%
		eSCN	0.179	11.11%
		EquiformerV2	0.172	10.77%
	Relaxation	SchNet	0.485	3.10%
		DimeNet++	0.496	3.23%
		PaiNN	0.225	9.10%
		GemNet-OC	0.174	12.18%
		eSCN	0.200	12.33%
		EquiformerV2	0.227	11.59%
		EquiformerV2 (large)	0.169	14.47%
test-ood(b)	Direct	GemNet-OC	0.220	7.13%
		eSCN	0.206	8.31%
		EquiformerV2	0.197	7.35%
	Relaxation	SchNet	0.621	1.64%
		DimeNet++	0.801	1.36%
		PaiNN	0.238	6.73%
		GemNet-OC	0.258	7.43%
		eSCN	0.289	9.54%
		EquiformerV2	0.276	6.96%
		EquiformerV2 (large)	0.179	8.98%
test-ood(l)	Direct	Gemnet-OC	0.220	8.84%
		eSCN	0.217	12.50%
		EquiformerV2	0.223	12.50%
	Relaxation	Schnet	0.621	3.72%
		Dimenet++	0.651	2.20%
		PaiNN	0.248	7.01%
		Gemnet-OC	0.244	8.19%
		eSCN	0.353	5.32%
		EquiformerV2	0.241	9.98%
		EquiformerV2 (large)	0.232	10.47%
test-ood(t)	Direct	GemNet-OC	0.494	4.05%
		eSCN	0.404	4.73%
		EquiformerV2	0.450	8.11%
	Relaxation	SchNet	1.040	0.62%
		DimeNet++	1.327	0.43%
		PaiNN	0.473	5.14%
		GemNet-OC	0.399	8.04%
		eSCN	0.440	7.23%
		EquiformerV2	0.441	6.39%
		EquiformerV2 (large)	0.366	8.15%
test-ood(lt)	Direct	GemNet-OC	0.385	6.68%
		eSCN	0.360	7.02%
		EquiformerV2	0.336	6.51%
	Relaxation	SchNet	0.711	2.05%
		DimeNet++	1.116	0.68%
		PaiNN	0.410	5.14%
		GemNet-OC	0.397	8.45%
		eSCN	0.463	5.10%
		EquiformerV2	0.414	6.56%
		EquiformerV2 (large)	0.405	9.87%



Table S10: Full results of metrics for IS2RS task on all data splits.

Initial Structure to Relaxed Structure ( <i>IS2RS</i> ) Test				
Split	Model	ADwT $\uparrow$	FbT $\uparrow$	AFbT $\uparrow$
test-id	GemNet-OC	85.46%	0.00%	6.53%
	eSCN	85.13%	0.40%	11.32%
	EquiformerV2	87.92%	0.00%	12.05%
	EquiformerV2 (large)	87.37%	0.60%	11.44%
test-ood(b)	GemNet-OC	87.79%	0.00%	4.54%
	eSCN	86.30%	0.60%	3.41%
	EquiformerV2	88.57%	0.00%	3.28%
	EquiformerV2 (large)	87.50%	0.40%	4.50%
test-ood(l)	GemNet-OC	69.74%	0.00%	1.97%
	eSCN	66.56%	0.40%	4.42%
	EquiformerV2	74.34%	0.00%	4.83%
	EquiformerV2 (large)	75.44%	0.00%	4.78%
test-ood(t)	GemNet-OC	60.03%	0.00%	0.95%
	eSCN	60.08%	0.00%	1.89%
	EquiformerV2	68.23%	0.00%	1.58%
	EquiformerV2 (large)	66.97%	0.20%	2.50%
test-ood(lt)	GemNet-OC	59.11%	0.00%	1.64%
	eSCN	61.27%	0.00%	3.54%
	EquiformerV2	68.30%	0.00%	3.27%
	EquiformerV2 (large)	65.58%	0.20%	2.32%